

University of São Paulo  
“Luiz de Queiroz” College of Agriculture

Obtaining and using aerial thermal images for the study of in-field crop spatial  
variability

**Matheus Gabriel Acorsi**

Dissertation presented to obtain the degree of Master in  
Science. Area: Agricultural Systems Engineering

Piracicaba  
2021

Matheus Gabriel Acorsi  
Agronomist

**Obtaining and using aerial thermal images for the study of in-field crop spatial variability**  
versão revisada de acordo com a resolução CoPGr 6018 de 2011

Advisor:  
Prof. Dr. **LEANDRO MARIA GIMENEZ**

Dissertation presented to obtain the degree of Master in  
Science. Area: Agricultural Systems Engineering

Piracicaba  
2021

**Dados Internacionais de Catalogação na Publicação**  
**DIVISÃO DE BIBLIOTECA – DIBD/ESALQ/USP**

Acorsi, Matheus Gabriel

Obtaining and using aerial thermal images for the study of in-field crop spatial variability / Matheus Gabriel Acorsi. - - versão revisada de acordo com a resolução CoPGr 6018 de 2011. - - Piracicaba, 2021.

61 p.

Dissertação (Mestrado) - - USP / Escola Superior de Agricultura “Luiz de Queiroz”.

1. Termografia 2. Estresse hídrico 3. Calibração 4. UAV 5. Sensoriamento remoto I. Título

*To my parents, Ana and Sidal*

**I DEDICATE**

## ACKNOWLEDGEMENTS

To the University of São Paulo – “Luiz de Queiroz” College of Agriculture, and the Graduate Program in Agricultural Engineering Systems for the opportunity to improve my knowledge in agricultural sciences.

To my parents, Ana and Sidali, for supporting me every step of the way especially during difficult times.

To my advisor, Professor Leandro Maria Gimenez, for all the assistance and mentoring throughout the development of this research, as well as, the friendship and countless advice.

To the Coordenação de Aperfeiçoamento de Pessoal de Nível Superior (CAPES) for the financial support through a scholarship granted.

To the Fundação de Estudos Agrários Luiz de Queiroz (FEALQ) for the financial support needed to the development of the research and for supporting publication fees.

To Fundação ABC, represented by Dr. Fabrício Povh, for all the assistance provided and for sharing the historic database of the field used in this study.

To Fazenda Uteva, especially Fábio Cunha, for granting free access to the field where this study was developed.

To Áureo Santana de Oliveira and Juarez Renó do Amaral, for all the technical assistance with electronic instrumentation.

To Professor Peterson Ricardo Fiorio, for lending us his own UAV platform multiple times.

To the Precision Agriculture Laboratory (LAP-ESALQ), for providing a significant part of the equipment used to develop this research.

To all the friends I made during the time I was at ESALQ, for all the support and memorable moments, making my stay in Piracicaba much easier and pleasant.

## CONTENTS

|   |    |
|---|----|
| RESUMO .....  | 7  |
| ABSTRACT .....  | 8  |
| 1. GENERAL INTRODUCTION .....   | 9  |
| REFERENCES .....  | 10 |
| 2. ASSESSING THE PERFORMANCE OF A LOW-COST THERMAL CAMERA IN<br>PROXIMAL AND AERIAL CONDITIONS..... | 13 |
| ABSTRACT .....  | 13 |
| 2.1. Introduction .....   | 13 |
| 2.2. Materials and Methods .....  | 15 |
| 2.2.1. Proximal analysis.....   | 16 |
| 2.2.2. Aerial analysis .....  | 17 |
| 2.2.2.1. Data acquisition .....   | 17 |
| 2.2.2.2. Flight altitude Analysis.....  | 19 |
| 2.2.2.3. Orthomosaic generation and blending modes analysis .....                                   | 20 |
| 2.2.3. Empirical line calibration .....   | 22 |
| 2.2.3.1. Proximal calibration .....   | 22 |
| 2.2.3.2. Aerial calibration .....   | 22 |
| 2.2.4. Statistical analysis .....   | 23 |
| 2.3. Results .....  | 23 |
| 2.3.1. Proximal analysis.....   | 23 |
| 2.3.2. Aerial analysis .....  | 24 |
| 2.3.2.1. Flight altitudes .....   | 24 |
| 2.3.2.2. Blending modes .....   | 27 |
| 2.3.2.3. Co-registration process .....  | 30 |
| 2.3.3. Calibration strategies .....   | 30 |
| 2.3.3.1. Proximal calibration .....   | 30 |
| 2.3.3.2. Aerial calibration .....   | 31 |
| 2.4. Discussion.....  | 33 |
| 2.5. Conclusions .....  | 37 |
| REFERENCES .....  | 37 |

|  |    |
|--|----|
| 3. PREDICTING SOIL WATER CONTENT AND MAIZE WATER STRESS THROUGH CANOPY TEMPERATURE IMAGERY ..... | 43 |
| ABSTRACT.....  | 43 |
| 3.1. Introduction.....   | 43 |
| 3.2. Materials and Methods.....  | 44 |
| 3.2.1. Study area.....   | 44 |
| 3.2.2. Guided sampling .....   | 45 |
| 3.2.3. UAV thermal imagery.....  | 45 |
| 3.2.4. Field data.....   | 47 |
| 3.2.4.1. Soil attributes .....   | 47 |
| 3.2.4.2. Plant attributes.....   | 48 |
| 3.2.4.3. Statistical analysis .....  | 48 |
| 3.3. Results.....  | 49 |
| 3.4. Discussion .....  | 56 |
| 3.5. Conclusion .....  | 58 |
| REFERENCES.....  | 59 |

## RESUMO

### Coleta e processamento de imagens termais para análise da variabilidade espacial de lavouras

O uso de cameras termográficas embarcadas em aeronaves remotamente pilotadas (RPA) expandiu as aplicações da termografia, sobretudo na agricultura, em que é demandada alta resolução espacial e temporal. Entretanto, obter medidas de temperatura acuradas a partir destes sensores nem sempre é trivial em virtude da instabilidade de sua acurácia e da dificuldade de produzir ortomosaicos a partir de imagens termais. Nesse sentido, superar esses problemas se mostra fundamental para garantir níveis de acurácia compatíveis com aplicações práticas, a exemplo da detecção do estresse hídrico das plantas, em que pequenas diferenças na temperatura do dossel podem refletir um princípio de estresse hídrico. Neste estudo, foi testada uma camera termográfica de baixo custo em condições proximais e aéreas, com enfoque no desenvolvimento de uma metodologia prática capaz de fornecer melhores níveis de acurácia nas leituras de temperatura, bem como, minimizar os problemas inerentes ao processamento fotogramétrico. Os resultados incluem um método de co-registro das imagens termais, capaz de mitigar os problemas enfrentados na etapa de alinhamento das imagens, favorecendo assim, a obtenção de ortomosaicos da área integral. Em termos de acurácia, foram desenvolvidos modelos de calibração de acordo com a altitude de voo e condições meteorológicas, elevando a acurácia final dos dados de temperatura para menos de 2 °C (root mean squared error - RMSE), com melhores resultados obtidos com a configuração de “blending mode” ajustada pela média. Essa metodologia foi posteriormente empregada para investigar a relação entre a temperatura do dossel das plantas coletada por meio das imagens aéreas com atributos relacionados ao estresse hídrico numa lavoura de milho em regime de sequeiro. Enquanto as imagens aéreas eram tomadas, efetuou-se uma amostragem direcionada ao longo da lavoura para que fossem coletados dados relativos ao teor de água na planta e no solo. Os resultados demonstraram que a área apresentava alta variabilidade no conteúdo de água no solo, com coeficiente de variação de 23.3 %, e valores de umidade volumétrica próximos aos de ponto de murcha permanente, confirmando a condição de déficit hídrico no solo. Tal resultado foi evidenciado nas medidas de temperatura do dossel, que variaram entre 32.8 até 40.6 °C entre os pontos amostrais. Apesar da temperatura do dossel das plantas ter apresentado correlação com a maioria dos atributos físicos do solo, os resultados da regressão linear simples entre temperatura e umidade volumétrica do solo atingiram coeficientes de determinação ( $R^2 \leq 0.26$ ), indicando que a temperatura do dossel não é suficiente para prever o conteúdo de água no solo. Apesar disso, quando a temperatura do dossel foi associada com alguns atributos físicos do solo em uma regressão linear múltipla, a capacidade preditiva do modelo foi elevada drasticamente, alcançando valores de  $R^2 \geq 0.83$ , o que demonstra a potencialidade do uso da temperatura das plantas em associação com dados pré-existentes de física do solo como ferramenta para análise da variabilidade espacial do teor de água no solo durante o ciclo da cultura.

Palavras-chave: RPA, Termografia, Camera termográfica, Conteúdo de água no solo, Estresse hídrico, Calibração

## ABSTRACT

**Obtaining and using thermal images for the study of in-field crop spatial variability**

The use of miniaturized thermal cameras attached to unmanned aerial vehicles (UAV) expanded the applications of remotely sensed temperature, especially in small-scale agriculture, where high spatial and temporal resolutions are necessary. However, deriving accurate temperature readings from these cameras is often challenging due to issues related to unstable accuracy and orthomosaic processing. Overcoming these problems is fundamental to ensure the accuracy needed for applications such as crop water stress monitoring, where small differences in canopy temperature (CT) can reflect an onset water stress. In this study, we tested a low-cost thermal camera in proximal and aerial conditions, focusing on developing a feasible methodology to deliver accurate temperature readings and mitigate issues related to orthomosaic processing. The results include a co-registering method that significantly increased the image alignment performance, producing suitable thermal orthomosaics. In terms of accuracy, calibration models were developed according to the flight altitude and conditions tested, resulting in root mean squared errors (RMSE) lower than 2 °C, with best results obtained with orthomosaics produced with blending mode set as average. Using this methodology, we investigated the relationship of UAV-based canopy temperature with soil and plant attributes linked to water status in a rainfed maize field. While the aerial images were taken, a guided sampling took place across the field to determine soil and plant water content. The results demonstrated that the field of study presented high spatial variability in terms of soil water storage (SWS), with a coefficient of variation of 23.3 % and values close to the permanent wilting point (PWP), confirming the soil water deficit. This result was reflected on CT values, which ranged from 32.8 to 40.6 °C among the sampling locations. Although CT correlated well with most of the soil physical attributes related to water dynamic, the simple linear regression between CT and soil water content variables yielded coefficients of determination ( $R^2$ )  $\leq 0.26$ , indicating that CT alone is not sufficient to predict soil water status. Nonetheless, when CT was combined with some soil physical attributes in a stepwise multiple linear regression the prediction capacity was significantly increased achieving  $R^2$  values  $\geq 0.83$ , demonstrating a potential use for CT associated with pre-existing soil attributes as an in-season tool to assess the spatial variability of soil water content.

Keywords: UAV, Thermography, Uncooled thermal camera, Soil water content, Plant water stress, Calibration

## 1. GENERAL INTRODUCTION

According to Williams (2014) Infrared thermography (IRT) is the science of acquisition, processing and analysis of thermal information from non-contact thermal sensors. These instruments are able to measure the emitted radiation from surface's objects in the long wave infrared (LWIR) electromagnetic spectrum (3 to 35  $\mu\text{m}$ ), exploiting the fact that every object with a temperature above absolute zero ( $-273.15\text{ }^{\circ}\text{C}$ ) emits radiation in the LWIR spectrum, with the amount of energy emitted being directly related to the object's kinetic temperature according to Plank's law (Prakash, 2000). For this reason, IRT has revolutionized the concept of temperature measurement, which was long dependent on instruments that could only perform pointwise measurements demanding direct contact with the material, such as thermocouples and thermometers (Vadivambal & Jayas, 2011).

Reflecting the recent advances in technology, thermal infrared cameras were significantly improved in terms of size and weight, which allowed these sensors to be attached to unmanned aerial vehicles (UAV) (Berni et al., 2009). The adoption of UAV-based thermal imagery promoted a wider range of applications, especially small-scale applications where high spatial and temporal resolution are needed, closing the gap between proximal and satellite-based thermal remote sensing (Colomina & Molina, 2014). Agriculture is one of the areas that have benefited from these advances, with aerial thermal images being used for plant phenotyping (Ludovisi et al., 2017), plant disease detection (Calderón et al., 2013), yield estimation (Feng et al., 2020) and crop water stress (Gago et al., 2015).

Although the miniaturization of thermal cameras promoted unprecedented advances in terms of applications, the lower accuracy offered by these cameras remains the major trade-off (Mesas-Carrascosa et al., 2018). To reduce the size and weight, miniaturized thermal cameras do not include an internal cooling system, being classified as uncooled thermal cameras for this reason. Once the sensor's sensitivity varies according to internal temperature, temperature readings are likely to change over time, introducing a source of error in these measurements (Olbrycht et al., 2012). Another issue that hampers the expansion of UAV-based thermal imagery is the difficult to produce orthomosaics. Because thermal images present a considerable low resolution and poor contrast, aligning overlapped images is often problematic, leading to imprecise orthomosaics (Hoffmann et al., 2016; Maes et al., 2017). Moreover, it is not clear if the configuration used during the mosaic processing can affect the final precision and accuracy of the temperature readings. Therefore, straightforward methodologies are necessary to overcome the aforementioned issues, focusing on delivering accurate temperature readings from suitable thermal orthomosaics.

According to Mesas-Carrascosa et al. (2018), plant water stress detection is one of the applications that can advance using accurate temperature measurements, which according to the authors, demands accuracy values around  $1\text{ }^{\circ}\text{C}$ . Such finesse is needed to detect the small changes in foliar temperature that occurs due to a water-saving mechanism, which reduces the transpiration in response to soil water deficit, leading to increases in canopy temperature (Jones, 2004). Hence, canopy temperature has been long used as a proxy to detect and quantify crop water stress (Idso et al., 1981), being successfully used as an irrigation management tool (Alderfasi & Nielsen, 2001; Quebrajo et al., 2018). Even though plant water stress is mainly caused by low soil water storage, very few studies explored the connection between crop water stress and soil attributes linked to its water holding capacity, with no studies yet reported investigating this relationship under a rainfed condition focusing on the spatial variability of these variables.

Within this context, in this study we investigated the performance of a low-cost uncooled thermal camera, focusing on optimizations during image acquisition and processing that could lead to better performance in terms of

overall accuracy and orthomosaic generation. Moreover, we used the developed methodology to investigate the relationship of UAV-based canopy temperature and maize water stress on a rainfed field by means of soil and plant water status variables sampled across the field.

## REFERENCES

- Alderfasi AA, Nielsen DC (2001) Use of crop water stress index for monitoring water status and scheduling irrigation in wheat. **Agricultural Water Management** 47:69-75
- Berni JAJ, Zarco-Tejada PJ, Suarez L, Fereres E (2009) Thermal and narrowband multispectral remote sensing for vegetation monitoring from an unmanned aerial vehicle. **IEEE Transactions on Geoscience and Remote Sensing** 47:722-738
- Calderón R, Navas-Cortés JA, Lucena C, Zarco-Tejada PJ (2013) High-resolution airborne hyperspectral and thermal imagery for early detection of Verticillium wilt of olive using fluorescence, temperature and narrow-band spectral indices. **Remote Sensing of Environment** 139:231-245
- Colomina I, Molina P (2014) Unmanned aerial systems for photogrammetry and remote sensing: A review. **ISPRS Journal of Photogrammetry and Remote Sensing** 92:79-97
- Feng A, Zhou J, Vories ED, Sudduth KA, Zhang M (2020) Yield estimation in cotton using UAV-based multi-sensor imagery. **Biosystems Engineering** 193:101-114
- Gago J, Douthe C, Coopman RE, Gallego PP, Ribas-Carbo M, Flexas J, Medrano H (2015) UAVs challenge to assess water stress for sustainable agriculture. **Agricultural Water Management** 153:9-19
- Hoffmann H, Nieto H, Jensen R, Guzinski R, Zarco-Tejada P, Friborg T (2016) Estimating evaporation with thermal UAV data and two-source energy balance models. **Hydrology and Earth System Sciences** 20:697-713
- Idso SB, Jackson RD, Pinter PJ, Reginato RJ, Hatfield JL (1981) Normalizing the stress-degree-day parameter for environmental variability. **Agricultural Meteorology** 24:45-55
- Jones HG (2004) Irrigation scheduling: advantages and pitfalls of plant-based methods. **Journal of Experimental Botany** 55:2427-2436
- Ludovisi R, Tauro F, Salvati R, Khoury S, Mugnozza Scarascia G, Harfouche A (2017) UAV-based thermal imaging for high-throughput field phenotyping of black poplar response to drought. **Frontiers in Plant Science** 8:1681
- Maes WH, Huete AR, Steppe K (2017) Optimizing the processing of UAV-based thermal imagery. **Remote Sensing** 9:476
- Mesas-Carrascosa FJ, Pérez-Porrás F, de Larriva JEM, Frau CM, Agüera-Vega F, Carvajal-Ramírez F, Martínez-Carricondo P, García-Ferrer A (2018) Drift correction of lightweight microbolometer thermal sensors on-board unmanned aerial vehicles. **Remote Sensing** 10:615
- Olbrycht R, Wiecek B, De Mey G (2012) Thermal drift compensation method for microbolometer thermal cameras. **Applied Optics** 51:1788-1794
- Prakash A (2000) Thermal Remote Sensing: Concepts, Issues and Applications. **International Archives of Photogrammetry and Remote Sensing** 33:239-243
- Quebrajo L, Perez-Ruiz M, Pérez-Urrestarazu L, Martínez G, Egea G (2018) Linking thermal imaging and soil remote sensing to enhance irrigation management of sugar beet. **Biosystems Engineering** 165:77-87
- Vadivambal R, Jayas DS (2011) Applications of thermal imaging in agriculture and food industry—a review. **Food and bioprocess technology** 4:186-199

Williams ME (2014) Repair of deteriorated bridge substructures using carbon fiber-reinforced polymer (CFRP) composites. In *Advanced Composites in Bridge Construction and Repair*. **Woodhead Publishing** pp.265-286



## 2. ASSESSING THE PERFORMANCE OF A LOW-COST THERMAL CAMERA IN PROXIMAL AND AERIAL CONDITIONS\*

### ABSTRACT

The development of low-cost miniaturized thermal cameras has expanded the use of remotely sensed surface temperature and promoted advances in applications involving proximal and aerial data acquisition. However, deriving accurate temperature readings from these cameras is often challenging due to the sensitivity of the sensor, which changes according to the internal temperature. Moreover, the photogrammetry processing required to produce orthomosaics from aerial images can also be problematic and introduce errors to the temperature readings. In this study, we assessed the performance of the FLIR Lepton 3.5 camera in both proximal and aerial conditions based on precision and accuracy indices derived from reference temperature measurements. The aerial analysis was conducted using three flight altitudes replicated along the day, exploring the effect of the distance between the camera and the target, and the blending mode configuration used to create orthomosaics. During the tests, the camera was able to deliver results within the accuracy reported by the manufacturer when using factory calibration, with a root mean square error (RMSE) of 1.08 °C for proximal condition and  $\leq 3.18^{\circ}\text{C}$  during aerial missions. Results among different flight altitudes revealed that the overall precision remained stable ( $R^2 = 0.94 - 0.96$ ), contrasting with the accuracy results, decreasing towards higher flight altitudes due to atmospheric attenuation, which is not accounted by factory calibration (RMSE = 2.63 – 3.18 °C). The blending modes tested also influenced the final accuracy, with the best results obtained with the average (RMSE = 3.14 °C) and disabled mode (RMSE = 3.08 °C). Furthermore, empirical line calibration models using ground reference targets were tested, reducing the errors on temperature measurements by up to 1.83 °C, with a final accuracy better than 2 °C. Other important results include a simplified co-registering method developed to overcome alignment issues encountered during orthomosaic creation using non-geotagged thermal images, and a set of insights and recommendations to reduce errors when deriving temperature readings from aerial thermal imaging.

**Keywords:** UAV, thermal infrared, calibration, thermal orthomosaic, thermography, uncooled thermal camera, FLIR Lepton, co-registration

### 2.1. Introduction

Monitoring surface temperature is important for many fields of science and technology, with applications ranging from a simple inspection of electronic components to climate change analysis using sea surface temperature data (SST). Most of these applications rely on remotely sensed measurements, in which temperature is derived from surface radiation emitted in the 8–14  $\mu\text{m}$  wavelengths and registered by thermal infrared (TIR) cameras (Prakash, 2000; Khanal et al., 2017; Baker et al., 2019). Since the 1970s, surface temperature can be monitored with worldwide coverage retrieving TIR data from satellite platforms, being constantly used in studies developed on a regional scale, such as hydrological modeling (Baker et al., 2019; Eschbach et al., 2017; Mundy et al., 2017), forest fire detection (Flasse & Ceccato, 1996; Quintano et al., 2017), and environmental monitoring (Kustas & Anderson, 2009). Within the last 20 years, the use of TIR cameras was expanded to proximal and aerial platforms reflecting technology advances with the

---

\* Current status: published. Available at:

Acorsi MG, Gimenez LM, Martello M (2020) Assessing the performance of a low-cost thermal camera in proximal and aerial conditions. **Remote Sensing** 12:3591. doi: 10.3390/rs12213591

development of cost-effective miniaturized thermal sensors (Aubrecht et al., 2016; Klemas, 2015; Berni et al., 2009). Some of these cameras are low power and lightweight enough to fit onto unmanned aerial vehicles (UAVs), with potential use for small-scale remote sensing where high spatial and temporal resolution is required (Berni et al., 2009; Colomina & Molina, 2014). Thermal imagery from UAVs has offered significant advances in agricultural applications, being used for plant phenotyping (Maimaitijiang et al., 2017; Natarajan et al., 2019; Perich et al., 2020), crop water stress detection (Gonzalez-Dugo et al., 2013; Martínez et al., 2017; Santesteban et al., 2017; Matese et al., 2018; Zhang et al., 2019; Crusiol et al., 2020), evapotranspiration estimation (Hoffmann et al., 2016), and plant disease detection (Calderón et al., 2013).

Although the miniaturization of thermal cameras was fundamental to expand the use of TIR data, this process ultimately affected the sensitivity and accuracy of these sensors (Mesas-Carrascosa et al., 2018). To reduce the size and weight, miniaturized thermal cameras do not include an internal cooling system, being classified as uncooled thermal cameras for this reason. Without a cooling mechanism, the internal temperature of the camera is susceptible to change during operation, affecting the sensitivity of the microbolometers that compose the sensor (focal plane array, FPA), which changes according to the internal temperature (Olbrycht et al., 2012). As a result, the temperature readings change with the FPA temperature (Nugent et al., 2013; Gómez-Candón et al., 2016), introducing errors in temperature measurements. This issue becomes more evident during UAV campaigns in which the camera may experience abrupt changes in internal temperatures due to wind and temperature drift during flight (Kelly et al., 2019). To minimize measurement bias caused by fluctuations in the FPA temperature, thermal cameras usually perform a non-uniformity correction (NUC) after a predefined time interval or temperature change by taking an image with the shutter closed (Olbrycht et al., 2012; Mesas-Carrascosa et al., 2018). Considering that the temperature is uniform across the shutter, the offset of each microbolometer is adjusted to ensure that further images will have a harmonized and accurate response signal (Olbrycht et al., 2012; Budzier & Gerlach, 2015). Because NUC is based on the assumption that the shutter temperature is equivalent to the rest of the camera interior, it is argued that it would not be valid for UAV imagery since the shutter mechanism is more susceptible to temperature drift due to the wind effect than other parts inside the camera (Kelly et al., 2019). Moreover, it is not clear if the frequency in which NUC is applied is enough to minimize sensor drift, especially for low-cost cameras that often do not allow adjustments on the NUC rate. For this reason, it is imperative that uncooled thermal cameras undergo a proper warm-up period before data acquisition to allow a temperature stabilization of FPA even when NUC is enabled (Berni et al., 2009; Nugent et al., 2013).

Other sources of errors that can also affect the performance of thermal cameras are target emissivity, the distance between the sensor and the target object, and atmospheric condition. While emissivity can be the main source of error when deriving temperature from TIR data (Aubrecht et al., 2016), it can easily be adjusted using reference values that are well-documented in the literature. On the other hand, the atmospheric attenuation of TIR radiation that affects airborne and orbital data demands more resources and might be more complex to correct (Torres-Rua, 2017). The atmospheric attenuation can cause large errors on temperature measurements (Meier et al., 2011; Hammerle et al., 2017), and is mainly affected by meteorological variables like air temperature and humidity along with the distance between the camera and target object (Torres-Rua, 2017). To correct temperature measurements, the amount of radiation attenuated by the atmosphere is estimated from radiative transfer models using meteorological data and the distance between the sensor and surface as input variables (Barsi et al., 2003; Kay et al., 2005). Although radiative transfer models are efficient, sometimes input data is not available and the method is often considered time-consuming (Torres-Rua, 2017). Therefore, calibration methods that present a straightforward

approach and account for more than one source of error are necessary to achieve accurate measurements, especially when deriving temperature from UAV thermal surveys.

Another important aspect of TIR UAV imagery is the image processing used to generate orthomosaics. Because such thermal cameras produce low resolution and poor contrast, the detection of common features among overlapped images performed during the alignment process becomes challenging, resulting in defective orthomosaics (Hoffmann et al., 2016; Dillen et al., 2016; Maes et al., 2017). To overcome this issue, some authors propose a co-registration process based on camera positions obtained from images captured simultaneously by a second camera that offers a higher resolution (usually a red blue green (RGB) or multispectral camera) (Raza et al., 2014; Yahyanejad & Rinner, 2015; Maes et al., 2017). In this case, the dataset from the second camera is processed first and the camera positions are then transferred to the corresponding thermal dataset, which significantly improves the alignment performance. In most cases, however, the thermal sensor is not coupled with a second camera or the simultaneous trigger is not possible, demanding alternative solutions. Moreover, the blending mode used to generate the orthomosaic can also influence the final results (Hoffmann et al., 2016; Perich et al., 2020). To assign pixel values, overlapping images with distinct viewing angles can be combined in different ways, based on the blending configuration (Aasen & Bolten, 2018). As a result, temperature values from the same target might change according to the blending mode. Although some studies have discussed the effects of the blending configuration on thermal data (Hoffmann et al., 2016; Kelly et al., 2019; Aragon et al., 2020; Perich et al., 2020), it has not been investigated how it can affect the overall precision and accuracy of temperature readings.

Within this context, in this study, we investigated the performance of a low-cost uncooled thermal camera, based on the precision and accuracy of temperature readings. We first assessed the proximal scenario, which aimed to analyze the Lepton camera under ideal conditions using factory calibration. Moreover, we investigated the camera performance on aerial conditions based on three flight altitudes conducted at different moments along the day. To overcome alignment issues, a co-registering method was proposed, and the orthomosaics produced were then evaluated according to the blending modes tested. Finally, we tested calibration models based on the ground reference temperature, aiming to reduce the residuals of temperature readings.

## 2.2. Materials and Methods

The study was designed to analyze the performance of the low-cost radiometric thermal camera FLIR Lepton 3.5 (FLIR Systems, Inc., Wilsonville, USA) in proximal and aerial conditions. As an original equipment manufacturer (OEM) sensor, FLIR Lepton 3.5 is designed to be built into a variety of electronic products (i.e., smartphones), requiring additional hardware and programming to properly work. The camera used in this study is based on an open-source project “DIY-Thermocam V2” developed by Ritter (2017), in which the Lepton module is connected to a Teensy 3.6 microcontroller (PJRC, Sherwood, USA), assembled on a printed circuit board along with a lithium-polymer battery (3.7 V, 2,000 mAh) and a touchscreen liquid crystal display (LCD). The Lepton sensor retail price is around \$200 (USD), with the final cost of building the prototype camera (hereafter referred to as Lepton camera) about \$400 (USD), which is at least three times less expensive than commercial solutions.

The Lepton camera features an uncooled VOx microbolometer FPA with a resolution of  $160 \times 120$  pixels and a spectral range of 8–14  $\mu\text{m}$ . Temperature readings are extracted from raw 14-bit images with a resolution of 0.05  $^{\circ}\text{C}$ . During the tests, the NUC was enabled with the default configuration, being performed on a three-minute interval or when the internal temperature exceeds 1.5  $^{\circ}\text{C}$  (FLIR, 2018).

Some other sensors were also used during the study to provide temperature reference measurements, enabling comparisons and further calibration procedures. Table 1 details the specifications of the sensors used to acquire temperature data.

**Table 1.** Detailed specifications of temperature sensors used during the study.

| Sensor                 | Detector Type                                 | Resolution | Detector Sensitivity | Field Of View | Spectral Range | Temperature Range | Reported accuracy       |
|------------------------|---|------------|----------------------|---------------|----------------|-------------------|-------------------------|
| <b>FLIR Lepton 3.5</b> | Focal Plane Array—Uncooled VOx Microbolometer | 160 × 120  | 0.05 °C              | 71° × 57°     | 8–14 μm        | −10 to +140 °C    | ±5 °C or 5 %            |
| <b>FLIR E5</b>         | Focal Plane Array—Uncooled Microbolometer     | 120 × 90   | 0.1 °C               | 45° × 34°     | 7.5–13 μm      | −20 to +250 °C    | ±2 °C or 2 %            |
| <b>MLX-90614BAA</b>    | Infra Red Sensitive Thermopile                | -          | 0.02 °C              | 10°           | -              | −70 to +380 °C    | ±0.5 °C (0 °C to 50 °C) |
| <b>Testo 926</b>       | Type T thermocouple (Cu-CuNi)                 | -          | 0.1 °C               | -             | -              | −50 to +400 °C    | ±0.3 °C                 |

### 2.2.1. Proximal analysis

To evaluate the precision and accuracy of temperature measurements obtained with the Lepton camera, an experiment under controlled conditions was setup using liquid water as a blackbody-like target (Baker et al., 2019). An FLIR E5 handheld camera (FLIR Systems, Inc., Wilsonville, USA) was also used for comparison purposes, placed in a tripod along with the Lepton camera facing perpendicularly a polystyrene box at a distance of 1 m. The polystyrene box was filled with water and a thermocouple (Testo 926, Testo SE & Co. KGaA, Lenzkirch, Germany) was attached at the side of the box, with the probe positioned parallel to the water surface at a 2 mm depth to record reference temperature data.

Data collection started after a 15-min stabilization time (Kelly et al., 2019), with both cameras being triggered simultaneously to capture a single image, repeating this process after increments in target temperature of approximately 1 °C over a range from 9.1 to 52.4 °C. Each increment on the target temperature was achieved by adding hot water to the polystyrene box, taking special care on the homogenization process, and then removing the same amount of water added to maintain a constant level. Reference temperature measurements were made based on the thermocouple readings, extracted according to the registration time of each image file. The experiment was repeated three times ( $n = 102$ ) and the laboratory temperature was kept stable at 22 °C.

Temperature data of FLIR E5 was extracted using FLIR Tools software (FLIR Systems, Inc., Wilsonville, USA), configured to adjust temperature data based on an emissivity of 0.99 (Buettner & Kern, 1965; Griggs, 1968), relative humidity of 80 %, air temperature of 22 °C, and target distance of 1 m. Average temperature values were obtained from each image using a box measurement tool, using pixels within the central portion of the polystyrene box. For images captured by the Lepton camera, temperature data was extracted using the open-source software ThermoVision (v. 1.10.0, Johann Henkel, Berlin, Germany). The software converts raw digital number values (DN) into temperature data based on a standard equation from the manufacturer (Eq. 1). To obtain the average temperature from each image, the same process used for FLIR E5 data was adopted, extracting the temperature values based on pixels located at the center portion of the reference target. It is worth mentioning that the boundary

boxes used to extract average temperature values from each camera had equivalent dimensions, covering approximately 3200 pixels, and remained in the same position throughout the analysis since both cameras were on attached to a fixed support.

$$\text{Temperature } (^{\circ}\text{C}) = 0.01DN - 273.15 \quad (\text{Eq. 1})$$

Furthermore, temperature values derived from each camera were combined with reference measurements in linear regression models, and the residuals calculated to assess the precision and accuracy of the sensors individually.

### 2.2.2. Aerial analysis

To explore the spatial and temporal variation of surface temperature, the use of thermal data is mostly based on orthomosaics, which are obtained through photogrammetric techniques applied to aerial imagery. In comparison to proximal approaches, aerial thermal imaging is more complex, and tends to have a lower degree of precision and accuracy due to the effect of environmental conditions and factors linked to dynamic data acquisition (Smigaj et al., 2016; Mesas-Carrascosa et al., 2018; Kelly et al., 2019; Aragon et al., 2020; Messina & Modica, 2020). In addition, image processing leading up to orthomosaic obtention can also influence the results and must be taken into account. To close these gaps, aerial data acquisition was conducted in distinct scenarios, covering different weather conditions and flight altitudes, followed by tests involving orthomosaic generation, calibration strategies, and their effect on the overall precision and accuracy of the Lepton camera.

#### 2.2.2.1. Data acquisition

UAV missions were conducted at the Biosystems Engineering Department of Luiz de Queiroz College of Agriculture—University of São Paulo (ESALQ-USP), Piracicaba, Brazil (Figure 1a). The Lepton camera was attached to a DJI Phantom 4 Advanced quadcopter (SZ DJI Technology Co., Shenzhen, China) using a custom-made 3D-printed fixed support, adjusted to collect close to nadir images. Three flight plans were used for image acquisition, based on each flight altitude tested: 35, 65, and 100 m. Prior to each mission, the camera was turned on at least 15 min before the flight to ensure that camera measurements were stable (Kelly et al., 2019). The image acquisition rate varied between 1.5 and 2 Hz among flights, corresponding to a forward overlap and side overlap of  $\geq 80\%$  and  $\geq 70\%$ , respectively, and flight speed limited to  $5 \text{ ms}^{-1}$ .

In order to capture a wider range of environmental conditions and target temperatures, the missions were performed in the early morning, close to solar noon, and at the end of the afternoon, with the three flight altitudes performed subsequently at each period, and cloudless conditions during all flights. More details regarding each mission and flight conditions are enlisted in Table 2.

**Table 2.** Flight mission details. AGL = Above Ground Level; GSD = Ground Sample Distance;  $T_{air}$  = Air temperature; RH = Relative humidity; SR = Shortwave Radiation.

| Mission ID | Date          | Start Time | Elapsed Time | N° of images | AGL | GSD                 | $T_{air}$ | RH   | SR                | Wind              |
|------------|---------------|------------|--------------|--------------|-----|---------------------|-----------|------|-------------------|-------------------|
|            |               |            |              |              | m   | cm px <sup>-1</sup> | °C        | %    | W m <sup>-2</sup> | m s <sup>-1</sup> |
| <b>A</b>   | 18 March 2020 | 7:18:10    | 11:06        | 1313         | 35  | 21.2                | 21.4      | 89.4 | 172.4             | 0.9               |
| <b>B</b>   | 18 March 2020 | 14:17:40   | 11:02        | 1302         | 35  | 21.9                | 31.5      | 53.3 | 583.4             | 1.3               |
| <b>C</b>   | 17 March 2020 | 17:27:10   | 11:06        | 1306         | 35  | 21.5                | 30.1      | 55.9 | 171.4             | 1.8               |
| <b>D</b>   | 18 March 2020 | 7:34:22    | 05:24        | 666          | 65  | 40.2                | 22.3      | 85.4 | 230.9             | 0.8               |
| <b>E</b>   | 18 March 2020 | 14:07:42   | 05:26        | 675          | 65  | 41.5                | 32.2      | 51.8 | 862.0             | 1.5               |
| <b>F</b>   | 17 March 2020 | 17:41:52   | 05:24        | 691          | 65  | 42.0                | 29.7      | 57.3 | 101.2             | 1.5               |
| <b>G</b>   | 18 March 2020 | 7:44:36    | 03:26        | 433          | 100 | 62.8                | 22.5      | 84.9 | 260.8             | 0.9               |
| <b>H</b>   | 18 March 2020 | 13:57:50   | 03:26        | 436          | 100 | 65.3                | 32.1      | 52.4 | 914.0             | 1.6               |
| <b>I</b>   | 17 March 2020 | 17:51:56   | 03:24        | 447          | 100 | 66.6                | 29.5      | 58.6 | 69.9              | 1.4               |

Reference measurements were obtained from seven targets distributed across the study area (Figure 1a). These targets were selected to cover a wide range of temperatures, different types of surfaces, and materials. Additionally, we only used targets covering at least 12 m<sup>2</sup> and with enough contrast to be distinguishable in the thermal images. The temperature of the targets was monitored during each flight using MLX90614 infrared sensors (hereafter referred to as the reference sensor) (Melexis, Ypres, Belgium) (Figure 1f). The reference sensor was installed with a nadir viewing angle 0.7 m above the target and connected to an Arduino microcontroller, recording temperature data at 5 s intervals. To ensure that reference temperature measurements were adjusted to an equivalent emissivity, the reference sensors were submitted to the protocol described in Section 2.2.2.1, in which an empirical line calibration was developed for each device using water as a blackbody-like target (Baker et al., 2019) ( $R^2_{val} = 0.999$ , RMSE = 0.28 °C). Even though the emissivity among the selected targets may vary, we decided to use a standard value since determining the emissivity of targets in the field was not feasible, and because using emissivity values reported in the literature would add an extra layer of uncertainty to the analysis.



**Figure 1.** Data acquisition scheme for aerial analysis. (a) Distribution and types of reference targets and ground control points; (b) Thermal image snapshot; (c) UAV platform with the Lepton camera onboard; (d) Lepton camera; (e) FLIR Lepton 3.5 OEM sensor; (f) Ground reference temperature platform with the MLX90614 sensor.

### 2.2.2.2. Flight altitude Analysis

The performance of the Lepton camera in aerial conditions was first assessed based on the flight altitudes tested during the study. Although the accuracy of temperature readings is expected to be reduced when increasing the flight level, it is important to quantify the magnitude of these deviations and evaluate the overall precision to make sure further calibration procedures are feasible.

To ensure that temperature readings were obtained in a more realistic perspective, individual images were used during the analysis. This ensured that temperature data were obtained without any processing that could change the original values. In addition, the number of samples used to perform statistical analysis was significantly higher, improving the robustness of the results. For each mission, six images per target were manually selected from the database. The selection criteria included three images from each flight direction, with the target located on the central portion of the images to avoid the vignetting effect (Hoffmann et al., 2016; Kelly et al., 2019; Aragon et al., 2020).

The selected images were first imported to the open-source software Thermal Data Viewer (Ritter, 2020), which converts in batch the proprietary files into a spreadsheet format (.CSV), and then converted into 14-bit TIFF images with DN values using R programming language (R Core Team, 2020). Furthermore, the TIFF images were

treated individually using ArcGIS software (v. 10.2.2, ESRI Ltd., Redlands, CA, USA). The first step was to set the spatial resolution according to the GSD from Table 2, ensuring that the pixel dimension was correct and in the metric system. Then, a circular buffer was used to extract the mean DN value, by visually locating the target and manually positioning the center point over the identified spot. Regarding the buffer size, a diameter of 1.6 m was used for all images, with average values derived from at least four pixels for missions conducted at a 100 m flying altitude, and a minimum of 11 and 43 pixels for the 65 and 35 m missions, respectively. Finally, the average DN value was converted into temperature data applying the factory model (Eq. 1), and then paired with the reference temperature using the time stamp of each image file.

### 2.2.2.3. Orthomosaic generation and blending modes analysis

Since the Lepton camera used in the study works independently from the UAV platform and does not produce geotagged images, additional steps were necessary prior to orthomosaic generation. This limitation is mainly caused by the inability of the camera to precisely record the time of each image acquisition and by fluctuations in the image capture rate, which makes the process of geotagging images using GNSS data from the UAV platform impractical. To solve this issue, a co-registering process was proposed and tested, in which the camera positions were estimated applying the structure from motion (SfM) algorithm to upscaled (pixel aggregation) thermal images with enhanced contrast. Through this process, the software can stitch overlapped images and generate a 3-D point cloud (Verhoeven, 2011), resulting in estimated camera positions when adding ground control points (GCPs).

To obtain the estimated camera positions for each dataset, we first excluded all images that were not within the flight plan (taking off, landing, maneuvering) along with blurry images and images with bands of dead pixels. The remaining images were then batch converted by Thermal Data Viewer into a JPEG format with an upscaled resolution and enhanced contrast. The software applies a bilinear interpolation increasing the original resolution to  $632 \times 466$  pixels and adjusts the contrast applying adaptive gamma correction. Furthermore, the images were loaded into Agisoft Photoscan Professional (v. 1.2.6, Agisoft LLC, St. Petersburg, Russia) and image alignment was performed with the following settings: accuracy set as the highest, pair selection as generic, standard key point limit of 20,000, and tie point limit of 1,000. If images were not aligned in the first attempt, these images were manually selected along with overlapped aligned images and realigned. After being aligned, five GCPs were added to the project, with coordinates previously measured with an RTK GNSS receiver (Topcon GR-3, 1 cm accuracy, Topcon Corporation, Tokyo, Japan). As GCPs targets, we used the roof corners' edge of buildings, which produced temperatures different enough from the surrounding targets to be distinguishable in thermal images. To reach the roof of the buildings, the GNSS receiver was attached to a telescopic pole, positioning the antenna right beside the roof corner. Finally, optimization of the camera alignment was performed, and the camera positions were exported.

To produce the orthomosaics of each mission, the same dataset used to estimate the camera positions was employed. However, in this case, the raw images were converted into 14-bit TIFF files, preserving the original resolution ( $160 \times 120$  pixels). This process was carried out by Thermal Data Viewer, exporting the proprietary files into a spreadsheet format (.CSV), and then converting into the TIFF format using R programming language. TIFF thermal images are composed of raw DN values and have reduced contrast, which, in addition to the low resolution of TIR sensors, affects the performance of SfM-based processing, especially if no camera positions are provided (Pech, 2013; Hoffmann et al., 2016; Dillen et al., 2016; Maes et al., 2017). When the image positions obtained in the last step were added, the alignment process was significantly improved as a result of a pre-selection of overlapped

images based on the coordinates of each image and the availability of the pitch-yaw-roll information. Moreover, the aforementioned GCPs were added to the project and the alignment optimization was executed, followed by the mesh generation. The final step was the orthomosaic creation, in which three orthomosaics were exported for each mission, based on the blending modes tested in the study: mosaic, average, and disabled. Other parameters available in Agisoft are the color correction, which was turned off, and the pixel size, which was adjusted to the maximum for all projects. An overview of all processing steps to obtain the orthomosaics is provided in Figure 2.

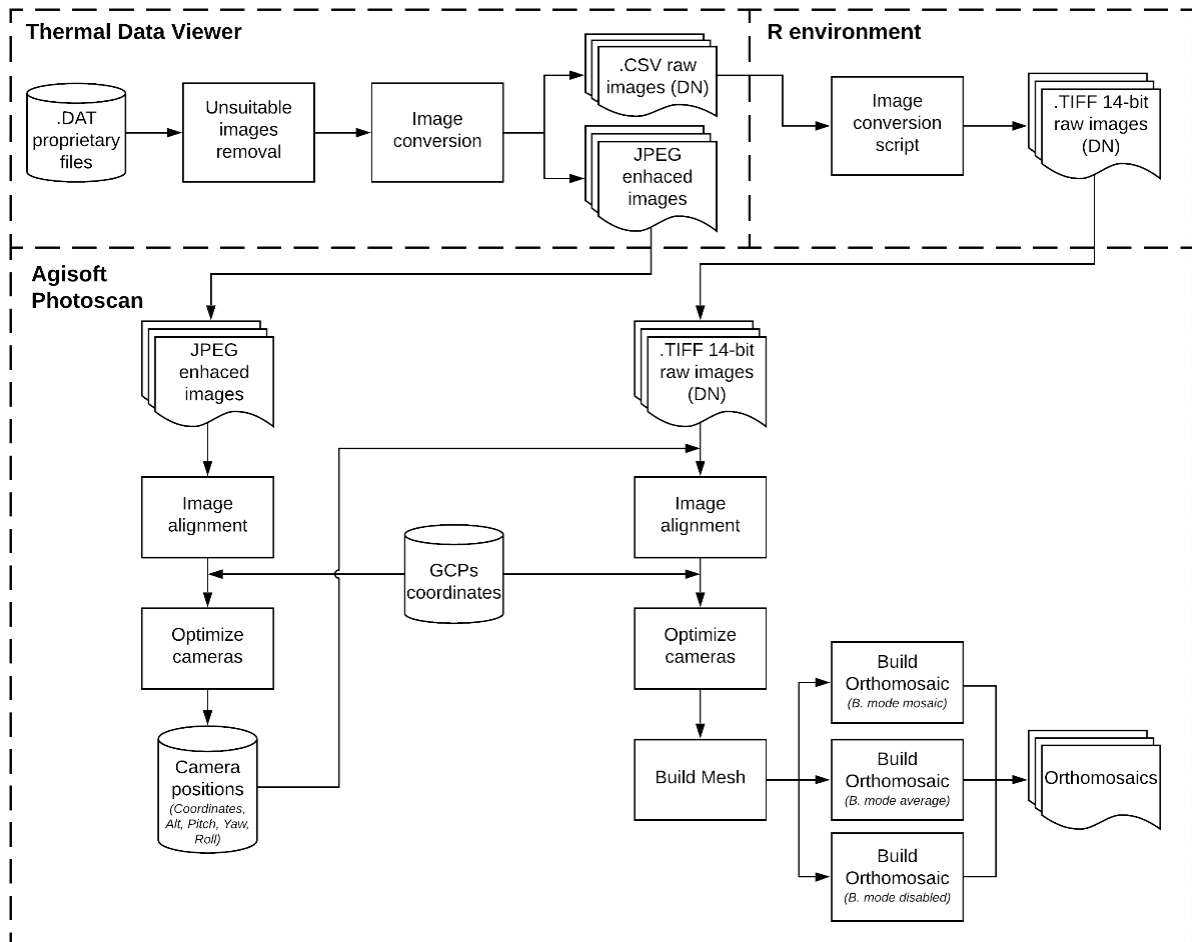


**Figure 2.** Overall flowchart for orthomosaics generation.

The extraction of temperature values from the orthomosaics representing each blending mode tested was carried out in ArcGIS software. Using the coordinates measured by the RTK-GNSS receiver from each target location, a buffer with a 1.6 m diameter was created. Then, using the zonal statistics tool, the average DN value was extracted using the pixels within the buffer of each target and converted to temperature data using the factory calibration model (Eq. 1), being later compared with reference temperature readings. To provide more reliable reference measurements, the average temperature was calculated considering the time interval in which each of the targets appears on the aerial images. This was achieved by manually selecting sequences of images depicting the target, and extracting temperature values from the reference sensor in these intervals to calculate the average reference temperature of the target.

### **2.2.3. Empirical line calibration**

#### **2.2.3.1. Proximal calibration**

To develop a proximal calibration model for the Lepton camera, the images collected during the proximal analysis (Section 2.2.2.1) were employed, with 70 % used to calibrate the model ( $n = 71$ ), and the remaining 30 % for validation ( $n = 31$ ), being selected to provide an equivalent range of temperature values for both steps. First, the average DN value was extracted from each image by the box measurement tool from ThermoVision software, using a fixed polygon to extract the pixel values within the central portion of the polystyrene box. The average DN values from images corresponding to the calibration step were then combined with reference temperature measurements on a linear regression model, which was later applied to convert DN data from images into temperature readings during the validation step. Furthermore, the temperature readings estimated through the linear regression model were compared with reference temperature data to evaluate the precision and accuracy of the calibration model developed.

#### **2.2.3.2. Aerial calibration**

Considering the wide range of conditions over the data acquisition from aerial analysis, being performed with different flight altitudes and at different times of the day, we developed multiple calibration models with different levels of specificity. The first model tested the performance of a general calibration model, based on a single dataset combining all flight altitudes and periods of the day analyzed in the study. Moreover, we also evaluated the performance of calibration models generated for specific conditions, with individual models for each flight altitude and periods of the day. In addition, the proximal calibration model obtained in Section 2.3.1 was also tested on aerial conditions to provide a parameter related to the atmospheric attenuation of TIR radiation.

To obtain the calibration models and properly compare the results, we first established a protocol that was used throughout the analysis. The dataset from the reference targets was separated into two groups, with four targets used for calibration (asphalt, brachiaria grass, clay tile roof, short grass) and the other three for the validation step (concrete, long grass, water) (Figure 1a). These targets were selected to provide the widest range of temperature values possible for the calibration and validation process, and were employed for all the models tested, ensuring that the different models were calibrated and validated with equivalent datasets from the same targets to promote fair comparisons.

All the calibration models were generated using individual images without any processing, based on the datasets obtained during the flight altitude analysis (Section 2.2.2.2). This way, we were able to increase the number of samples used to calibrate the models and avoided introducing any uncertainties from the orthomosaic processing, adding robustness to the method. To extract the average DN value from each image used for calibration, the same procedure described in the third paragraph of Section 2.2.2.2 was used, in which a buffer with a 1.6 m diameter was manually positioned over the target location to extract the mean DN value and then paired with the reference temperature according to the timestamp of the image. Moreover, the datasets were organized accordingly and used to build the linear regression model of each strategy mentioned above.

To test the linear regression models obtained, we decided to use the orthomosaics instead of individual images, since the majority of users extract temperature data from aerial thermal images through orthomosaics. In addition, we decided to use only the orthomosaics generated by the blending mode that provided the best precision

and accuracy during our tests, aiming to reproduce the best scenario to test calibration models. To calculate the average DN value from targets selected for validation, the method described in the fourth paragraph of Section 2.2.2.3 was used, with raw DN data extracted from a 1.6 m circular buffer positioned over the target location based on coordinates measured by an RTK-GNSS receiver. The average DN value from each target was then converted into temperature applying the corresponding linear regression model previously obtained, and paired with reference temperature measurements calculated considering the time interval in which the target appears on the aerial images used to build the orthomosaic.

#### **2.2.4. Statistical analysis**

To assess the performance of the Lepton camera, we compared the thermal temperature data with reference temperature readings, analyzing the relationship between the measurements and the residuals. The precision of the camera was evaluated using the coefficient of determination values ( $R^2$ ), whereas the accuracy was assessed based on the residuals analysis, represented by the mean error (ME), mean absolute error (MAE), root mean square error (RMSE), and the relative root mean square error (rRMSE). The same methodology was used to assess the performance of the calibration strategies, extracting the coefficients mentioned above from the residuals of the validation step, and calculating the  $R^2$  value along with the significance level from the regression model obtained in the calibration step.

### **2.3. Results**

#### **2.3.1. Proximal analysis**

Temperature readings from the thermal cameras presented a strong relationship with the reference temperature data, with  $R^2$  values higher than 0.99 (Figure 3), indicating that these devices provide high-precision measurements in the temperature range (9.1 to 52.4 °C) and conditions tested.

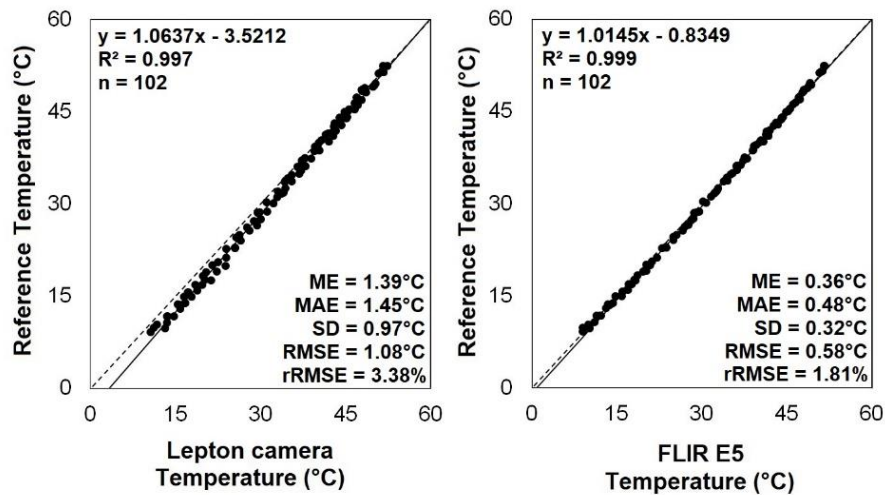


**Figure 3.** Linear regression models between TIR temperature and reference temperature readings for the Lepton camera and FLIR E5. Dashed line = 1:1 line; solid line = linear regression line; n = number of samples;  $R^2$  = coefficient of determination; ME = mean error; MAE = mean absolute error; RMSE = root mean square error; rRMSE = relative RMSE  $p < 0.001$  for all  $R^2$ .

In terms of accuracy, the cameras were distinct. The Lepton camera temperature readings had higher residuals, with MAE of 1.45 °C and RMSE of 1.08 °C, whereas the FLIR E5 results were 0.48 and 0.58 °C, respectively. When compared to the average reference temperature, rRMSE from the Lepton camera represents 3.38 %, and 1.81 % for FLIR E5.

## 2.3.2. Aerial analysis

### 2.3.2.1. Flight altitudes

Based on the overall results (Table 3), the relationship between the thermal data and reference temperature, expressed by the  $R^2$  values, was similar, demonstrating that the precision of TIR measurements was not affected by the flight altitudes tested in the study. On the other hand, the results related to the residuals, which express the accuracy of the camera readings, were slightly different between missions. Datasets collected at 35 m yielded the lowest residuals, with an overall RMSE of 2.63 °C (rRMSE = 8.35 %). Missions conducted at 65 and 100 m presented nearly the same accuracy, with RMSE of 3.15 and 3.18 °C (rRMSE of 9.96 % and 10.04 %), respectively.

**Table 3.** Relationship and residuals between TIR measurements and reference temperature for aerial conditions according to flight altitudes tested. n = number of samples; R<sup>2</sup> = coefficient of determination; ME = mean error; MAE = mean absolute error; RMSE = root mean square error; rRMSE = relative RMSE; p-value < 0.001 (\*\*).

| Flight altitude (m) | Mission ID | n   | R <sup>2</sup> | ME    | MAE  | SD   | RMSE | rRMSE |
|---------------------|------------|-----|----------------|-------|------|------|------|-------|
|                     |            |     |                | °C    |      |      |      | %     |
| 35                  | A          | 42  | 0.62**         | 0.24  | 1.90 | 1.49 | 2.41 | 10.70 |
|                     | B          | 42  | 0.95**         | -1.28 | 2.32 | 1.49 | 2.75 | 7.09  |
|                     | C          | 42  | 0.85**         | -1.69 | 2.26 | 1.54 | 2.72 | 8.19  |
|                     | Overall    | 126 | 0.94**         | -0.91 | 2.16 | 1.51 | 2.63 | 8.35  |
| 65                  | D          | 42  | 0.75**         | -0.17 | 1.65 | 1.25 | 2.06 | 8.71  |
|                     | E          | 42  | 0.98**         | -2.63 | 2.91 | 2.60 | 3.88 | 9.64  |
|                     | F          | 42  | 0.82**         | -1.72 | 2.61 | 1.94 | 3.24 | 10.43 |
|                     | Overall    | 126 | 0.95**         | -1.50 | 2.39 | 2.06 | 3.15 | 9.96  |
| 100                 | G          | 42  | 0.74**         | -0.22 | 1.85 | 1.25 | 2.23 | 9.23  |
|                     | H          | 42  | 0.98**         | -2.15 | 3.57 | 2.71 | 4.47 | 10.99 |
|                     | I          | 42  | 0.96**         | -0.22 | 1.94 | 1.30 | 2.33 | 7.69  |
|                     | Overall    | 126 | 0.96**         | -0.87 | 2.46 | 2.03 | 3.18 | 10.04 |

Information about each flight mission is presented in Table 2.

Contrasting with the overall results reported, the 35-m flight had the weakest performance among missions carried out in the early morning (A, D, and G), with an R<sup>2</sup> of 0.62 and RMSE = 2.41 °C, being the only mission in which TIR temperature was overestimated (ME > 0) in relation to reference values. Results from the 65 and 100 m flight altitudes also produced weaker results in terms of precision for early morning missions, with R<sup>2</sup> values of 0.75 and 0.74, respectively. However, the best accuracy values were observed in this condition, with RMSE ranging from 2.06 (mission D) to 2.41 °C (mission A), indicating that the lower R<sup>2</sup> values might be linked to the smaller temperature range.

Regarding the linear regression models generated (Figure 4), different patterns of slope and intercept values were observed according to the flight altitudes tested. Based on overall models and the range of temperature analyzed, the slope tends to increase and the intercept to decrease when elevating the flight altitude, indicating that low temperatures would be gradually overestimated and high temperature underestimated when increasing the flight altitude and deriving TIR temperature using the factory calibration.

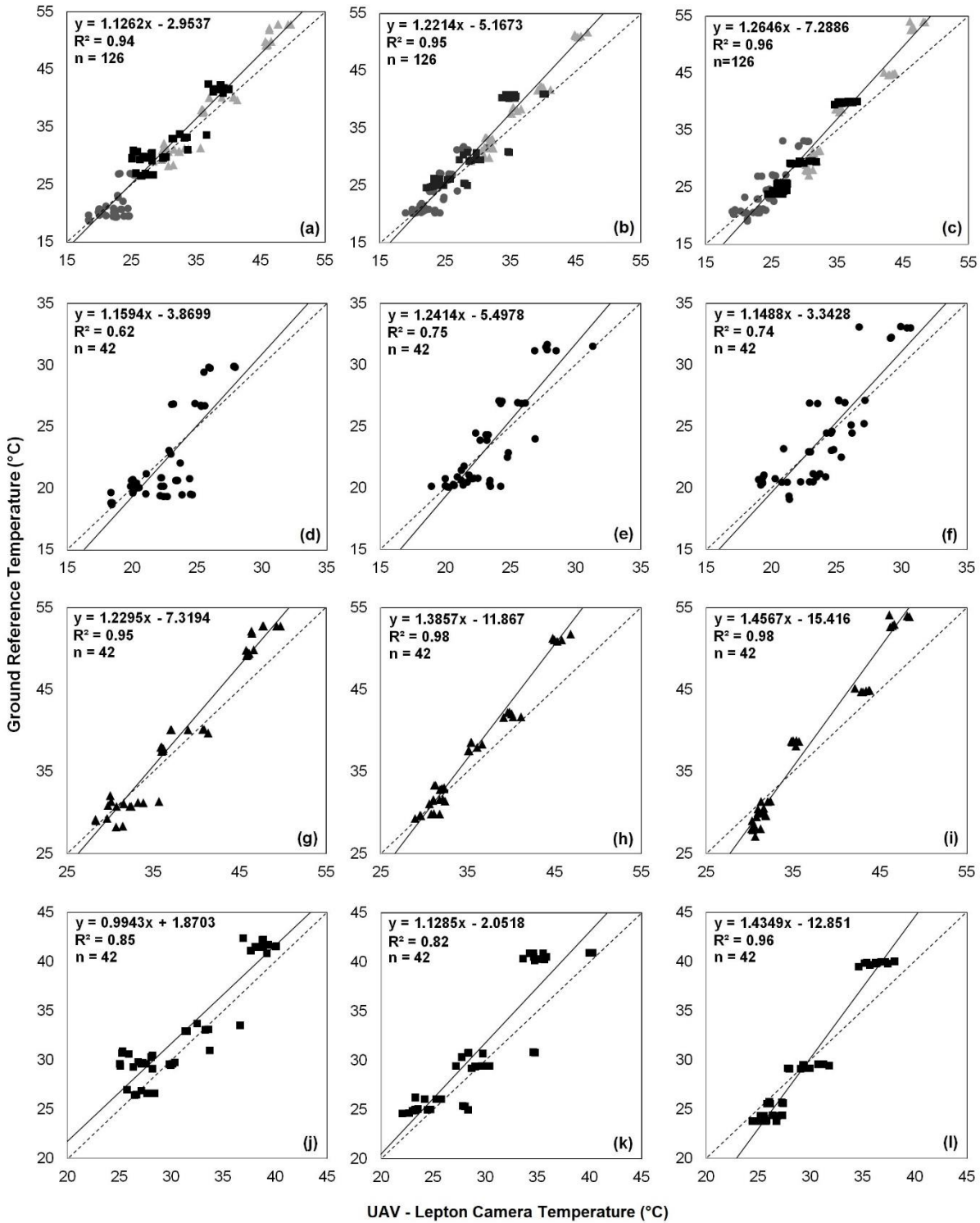


**Figure 4.** Linear regression models between temperature readings from the Lepton camera and ground reference temperature throughout the missions in different flight altitudes. Overall models for the 35 (a), 65 (b), and 100 m flight altitudes (c); individual models for the 35 (d, g, j), 65 (e, h, k), and 100 m flight altitudes (f, i, l); symbols indicate datasets collected in the early morning (●), close to solar noon (▲), and at the end of the afternoon (■). Dashed line = 1:1 line; solid line = linear regression line;  $p < 0.001$  for all  $R^2$ .

### 2.3.2.2. Blending modes

The performance of blending modes was assessed based on missions from the 65 and 100 m flight altitudes. Datasets from the 35 m missions (A, B, and C) were not included in the analysis because the orthomosaic from mission A could not be properly generated, and using only the two remaining orthomosaics would compromise the comparison with results from other flight altitudes. The orthomosaic was not successfully generated because some images covering a significant part of the area of study could not be aligned and further covered by the orthomosaic. Since the 35 m missions take at least twice the time required by other flight altitudes to complete image acquisition and targets in the early morning particularly experience dramatic increases in temperature values (Figure 5a), the process of stitching images performed by the SfM algorithm might be affected, because DN values from the same object extracted of images derived of a parallel flight line can change abruptly, and the algorithm may not recognize that these two values belong to the same target. This problem was not experienced in other missions using the 35 m data (mission B, C), probably because the targets' temperature was more stable in these conditions (Figure 5b,c).

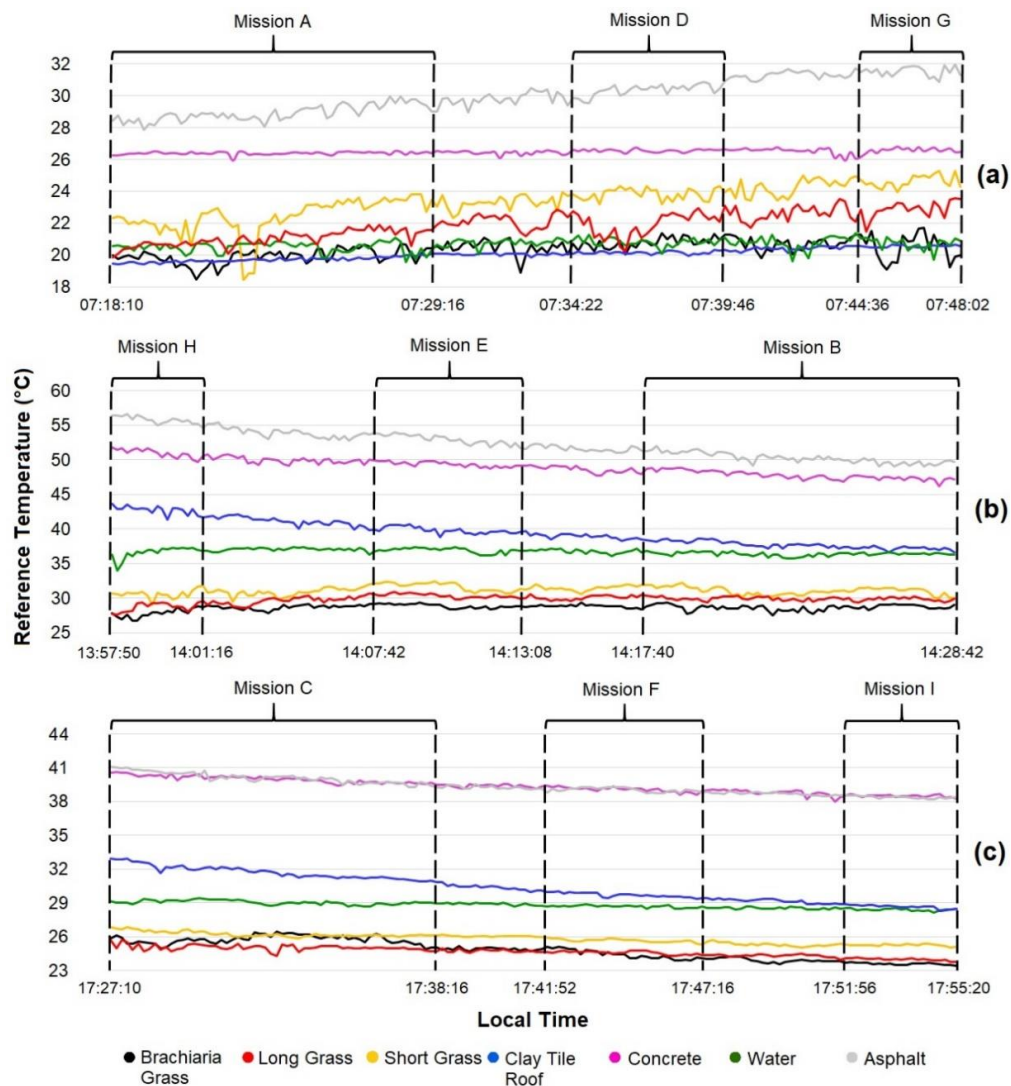


**Figure 5.** Ground reference temperature from validation targets across all missions. Missions conducted in the early morning (a), close to solar noon (b), and at the end of the afternoon (c).

The overall results, which combine datasets from the 65 and 100 m flight altitudes, indicate that the mosaic mode had the weakest performance, with an  $R^2 = 0.92$  and RMSE of 3.93 °C (rRMSE = 12.43 %) (Table 4). The average blending mode and the disabled option yielded the best precision values, with an overall  $R^2$  of 0.96 in both cases. The accuracy was also similar, with an RMSE of 3.14 °C (rRMSE = 9.93 %) for the average mode, and equal to 3.08 °C (rRMSE = 9.74 %) with the blending mode disabled.

**Table 4.** Relationship and residuals between the temperature extracted from the orthomosaics and the reference temperature for aerial conditions according to the blending modes tested. n = number of samples;  $R^2$  = coefficient of determination; ME = mean error; MAE = mean absolute error; RMSE = root mean square error; rRMSE = relative RMSE; p-value < 0.001 (\*\*); p-value < 0.01 (\*).

| Blending Mode | Mission ID | n  | Model                | $R^2$  | ME    | MAE  | SD   | RMSE | rRMSE |
|---------------|------------|----|----------------------|--------|-------|------|------|------|-------|
|               |            |    |                      |        | °C    |      |      | %    |       |
| Mosaic        | D          | 7  | $y = 1.637x - 14.43$ | 0.87*  | -0.34 | 1.67 | 1.31 | 2.07 | 8.78  |
|               | E          | 7  | $y = 1.888x - 30.83$ | 0.95** | -2.56 | 4.01 | 3.98 | 5.45 | 13.57 |
|               | F          | 7  | $y = 1.764x - 22.48$ | 0.96** | -0.67 | 2.59 | 1.75 | 3.05 | 9.86  |
|               | G          | 7  | $y = 1.769x - 16.53$ | 0.95** | -1.15 | 1.62 | 1.81 | 2.33 | 9.64  |
|               | H          | 7  | $y = 1.814x - 28.10$ | 0.97** | -2.72 | 4.86 | 3.74 | 5.97 | 14.71 |
|               | I          | 7  | $y = 1.798x - 24.10$ | 0.99** | 0.00  | 2.48 | 1.57 | 2.88 | 9.52  |
|               | Overall    | 42 | $y = 1.341x - 9.13$  | 0.92** | -1.24 | 2.87 | 2.36 | 3.93 | 12.43 |
| Average       | D          | 7  | $y = 1.551x - 12.56$ | 0.97** | -0.26 | 1.20 | 1.12 | 1.58 | 6.73  |
|               | E          | 7  | $y = 1.369x - 11.89$ | 0.97** | -2.13 | 2.37 | 3.01 | 3.66 | 9.11  |
|               | F          | 7  | $y = 1.317x - 8.01$  | 0.96** | -1.38 | 1.66 | 1.90 | 2.42 | 7.81  |
|               | G          | 7  | $y = 1.602x - 13.91$ | 0.94** | -0.39 | 1.36 | 1.45 | 1.91 | 7.89  |
|               | H          | 7  | $y = 1.508x - 16.82$ | 0.98** | -2.52 | 3.92 | 3.02 | 4.81 | 11.86 |
|               | I          | 7  | $y = 1.495x - 14.02$ | 0.84*  | -0.68 | 2.56 | 2.16 | 3.25 | 10.75 |
|               | Overall    | 42 | $y = 1.264x - 6.80$  | 0.96** | -1.23 | 2.18 | 2.11 | 3.14 | 9.93  |
| Disabled      | D          | 7  | $y = 1.414x - 9.19$  | 0.94** | -0.39 | 1.22 | 1.03 | 1.55 | 6.59  |
|               | E          | 7  | $y = 1.401x - 12.32$ | 0.99** | -2.71 | 3.01 | 2.65 | 3.88 | 9.67  |
|               | F          | 7  | $y = 1.087x - 0.96$  | 0.78*  | -1.61 | 2.77 | 2.18 | 3.43 | 11.09 |
|               | G          | 7  | $y = 1.365x - 8.06$  | 0.84*  | -0.55 | 1.65 | 1.34 | 2.06 | 8.53  |
|               | H          | 7  | $y = 1.449x - 15.18$ | 0.98** | -2.11 | 3.48 | 2.67 | 4.26 | 10.51 |
|               | I          | 7  | $y = 1.386x - 10.64$ | 0.96** | -0.73 | 1.73 | 1.58 | 2.26 | 7.49  |
|               | Overall    | 42 | $y = 1.233x - 5.71$  | 0.96** | -1.35 | 2.31 | 1.91 | 3.08 | 9.74  |

Information about each flight mission is presented in Table 2.

Analyzing the overall regression models obtained according to the blending mode used (Figure 6), the slope and intercept values were similar to those obtained in the flight altitude assessment. The model generated using the mosaic blending mode was slightly different than the others, with a higher value for the slope and lower intercept, meaning that low temperatures would be more overestimated and high temperatures underestimated, compromising the accuracy. The average mode and the disabled option resulted in very similar regression models, with comparable slope and intercept values, closer to the 1:1 line.

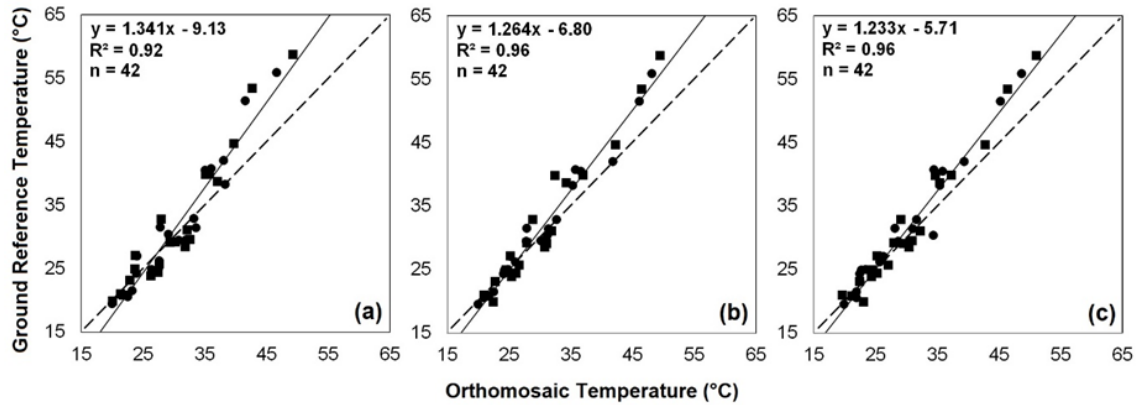


**Figure 6.** Linear regression models between the ground reference temperature and TIR temperature from orthomosaics obtained with the mosaic (a) and averaged (b) blending modes, and with blending disabled (c). Symbols indicate datasets from 65 (●) and 100 m (■) flight altitudes. Dashed line = 1:1 line; solid line = linear regression line;  $p < 0.001$  for all  $R^2$ .

Besides the differences in terms of statistical results, the contrast between the blending configurations tested is even more evident when comparing the visual results from the orthomosaics. A zoomed view of the area is shown in Figure 7, illustrating the effect of the blending modes used by showing temperature values' variation across a transect drawn on the orthomosaics corresponding to the mosaic mode (Figure 7a), average (Figure 7b), and disabled option (Figure 7c). The visual difference is more evident for the average and the disabled mode, in which a smoother characteristic is observed for the average one, whereas the mosaic and disabled option present more contrast between transitions in temperature values, giving the impression of enhanced detail. Additionally, when the blending mode is disabled, we can notice the presence of seamlines between images used to obtain the orthomosaic, with abrupt changes in temperature values along the transect profile. Differences in terms of accuracy are also visible when comparing the temperature values from orthomosaics with the reference values of ground reference targets depicted in Figure 7, with a higher discrepancy for mosaic mode values in relation to the average and the disabled option.

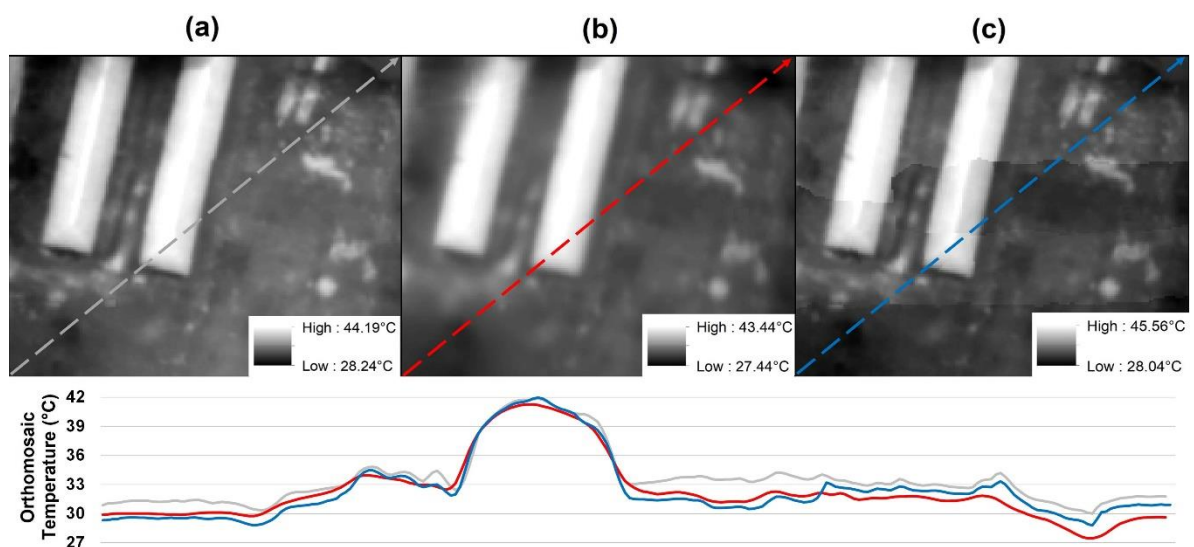


**Figure 7.** Zoomed view of the area based on orthomosaics from mission E with mosaic (a) and averaged (b) blending modes, and with blending disabled (c). The profile graph illustrates temperature values along the transect from orthomosaics using the blending modes tested.

### 2.3.2.3. Co-registration process

The proposed co-registering method was fundamental to overcome the alignment issues encountered with non-geotagged thermal images during the photogrammetry process. Without camera positions, an average of 37 % of the images were properly aligned, with an overall of 1,516 and 833 tie points for missions conducted at the 65 and 100 m flight altitude, respectively. When the camera positions generated were added to the project, the percentage of aligned images more than doubled, reaching an average value of 84.7 %. The overall number of tie points also increased, with an average of 3,806 points for the 65 m missions, and 1,724 points with missions from the 100 m flight altitude. Detailed information is presented in Table 5.

**Table 5.** Results from the alignment step of the orthomosaic processing with and without the use of camera positions obtained with the co-registering method.

| Mission ID | Number of photos | Without co-registering |            | With co-registering |            |
|------------|------------------|------------------------|------------|---------------------|------------|
|            |                  | Aligned photos (%)     | Tie points | Aligned photos (%)  | Tie points |
| D          | 527              | 46.1                   | 1978       | 79.7                | 4294       |
| E          | 518              | 38.6                   | 1396       | 89.4                | 3499       |
| F          | 543              | 25.2                   | 1175       | 81.4                | 3625       |
| Overall    | -                | 36.7                   | 1516       | 83.5                | 3806       |
| G          | 350              | 51.7                   | 1075       | 87.4                | 1940       |
| H          | 346              | 28.0                   | 526        | 83.2                | 1544       |
| I          | 339              | 31.9                   | 898        | 87.0                | 1687       |
| Overall    | -                | 37.2                   | 833        | 85.9                | 1724       |

Information about each flight mission is presented in Table 2.

## 2.3.3. Calibration strategies

### 2.3.3.1. Proximal calibration

The calibration model generated with 70 % of the proximal dataset, combining the DN values from raw images and the reference temperature, yielded an  $R^2$  of 0.997 (Figure 8a). The residuals extracted from the remaining 30 % of the data resulted in an MAE of 0.69 °C and RMSE = 0.80 °C, equivalent to 2.52 % (rRMSE) (Figure 8).

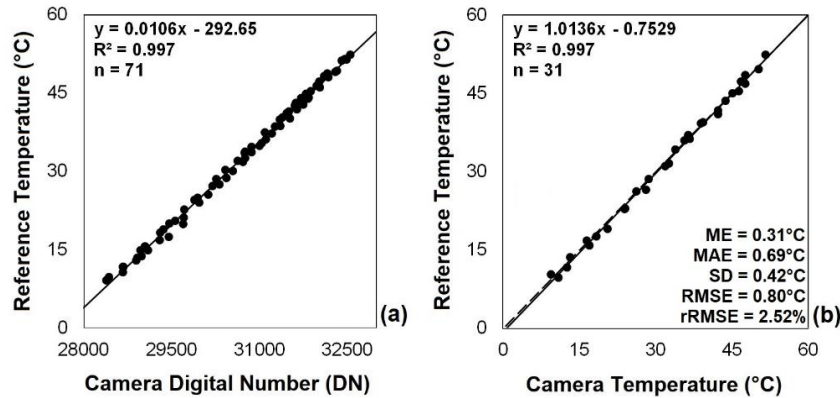


**Figure 8.** Linear regression models of the proximal calibration analysis. (a) calibration model between DN values extracted from raw images and reference temperature data; (b) validation model between TIR calibrated temperature and reference data. Dashed line = 1:1 line; solid line = linear regression line;  $n$  = number of samples;  $R^2$  = coefficient of determination; ME = mean error; MAE = mean absolute error; RMSE = root mean square error; rRMSE = relative RMSE;  $p < 0.001$  for all  $R^2$ .

### 2.3.3.2. Aerial calibration

Since the average and disabled mode had equivalent results terms of precision and accuracy, we decided to use datasets obtained with the average blending mode to avoid issues related to the abrupt changes in temperature values observed in orthomosaics made with disabled blending, as described in Section 2.3.2.2.

The first calibration strategy tested used the model obtained from the proximal analysis (Section 2.3.3.1) in aerial conditions, based on missions from the 65 and 100 m flight altitudes. The residuals, which correspond to the accuracy degree, were the highest observed, with an RMSE of 3.40 °C (rRMSE = 10.71 %) (Table 6). Additionally, the ME was the lowest observed, corresponding to  $-2.75$  °C, indicating that temperature values corrected by this model would be underestimated. The general model, which was generated combining aerial images from the 65 and 100 m missions, had an  $R^2$  of 0.95 for the calibration dataset and yielded the best accuracy based on the residuals from the validation step, with RMSE of 1.31 °C (rRMSE = 4.12 %). Other two models were generated and validated using individual datasets from the 65 and 100 m missions, resulting in residuals slightly higher than the ones obtained with the general model. The 65 m model produced an RMSE of 1.56 °C (rRMSE = 4.93 %), whereas the 100 m model yielded an RMSE equal to 1.32 °C (rRMSE = 4.16 %). The last strategy tested was the calibrating temperature using models generated specifically for each time of the day data acquisition took place, with calibration models developed for early morning, noon, and the end of afternoon, and validated with corresponding datasets. In terms of accuracy, this strategy provided the lowest performance among calibrations based on aerial images, with RMSE ranging from 1.57 to 1.94 °C (rRMSE between 4.81 % and 6.74 %). In addition, temperature values calibrated by these models were underestimated ( $ME < 0$ ), a characteristic that was not present in other aerial calibration models. This effect can be clearly observed in Figure 9, in which the result of different calibration models on temperature readings is illustrated in the profile graph, combining orthomosaics calibrated with factory (Figure 9a), proximal (Figure 9b), and general calibration (Figure 9c), whereby the factory and proximal models underestimate temperature, whilst the general model yields more accurate readings.

**Table 6.** Cross-validation results between the DN values of orthomosaics and the ground reference temperature based on different datasets. n = number of samples; R<sup>2</sup> = coefficient of determination; ME = mean error; MAE = mean absolute error; RMSE = root mean square error; rRMSE = relative RMSE; p-value < 0.001 (\*\*); p-value < 0.01 (\*).

| Method                | Calibration |                    |                | Validation |                |       |      |      |      |       |
|-----------------------|-------------|--------------------|----------------|------------|----------------|-------|------|------|------|-------|
|                       | n           | Model              | R <sup>2</sup> | n          | R <sup>2</sup> | ME    | MAE  | SD   | RMSE | rRMSE |
|                       |             |                    |                |            |                | °C    |      |      |      |       |
| Proximal <sup>a</sup> | 71          | y=0.0106x - 292.65 | 0.99**         | 18         | 0.98**         | -2.75 | 2.81 | 1.96 | 3.40 | 10.71 |
| General <sup>b</sup>  | 180         | y=0.0125x - 347.39 | 0.95**         | 18         | 0.98**         | 0.15  | 0.99 | 0.87 | 1.31 | 4.12  |
| 65 m <sup>c</sup>     | 90          | y=0.0122x - 337.21 | 0.95**         | 9          | 0.99**         | 1.28  | 1.29 | 0.93 | 1.56 | 4.93  |
| 100 m <sup>d</sup>    | 90          | y=0.0129x - 359.05 | 0.96**         | 9          | 0.99**         | 0.57  | 1.23 | 1.26 | 1.32 | 4.16  |
| 7-8h <sup>e</sup>     | 60          | y=0.0126x - 351.29 | 0.76**         | 6          | 0.94*          | -1.34 | 1.34 | 0.90 | 1.57 | 6.74  |
| 13-14h <sup>f</sup>   | 60          | y=0.0144x - 408.19 | 0.98**         | 6          | 0.98**         | -1.27 | 1.46 | 1.41 | 1.94 | 4.81  |
| 17-18h <sup>g</sup>   | 60          | y=0.0124x - 346.06 | 0.86**         | 6          | 0.98**         | -1.35 | 1.60 | 0.57 | 1.68 | 5.37  |

Calibration model obtained with: <sup>a</sup>datasets from proximal analysis; <sup>b</sup>datasets from the 65 and 100 m flight altitude; <sup>c</sup>datasets from the 65 m flight altitude; <sup>d</sup>datasets from the 100 m flight altitude; <sup>e</sup>datasets collected in the early morning; <sup>f</sup>datasets collected close to solar noon; <sup>g</sup>datasets collected at the end of the afternoon. More information about each flight mission is presented in Table 2.

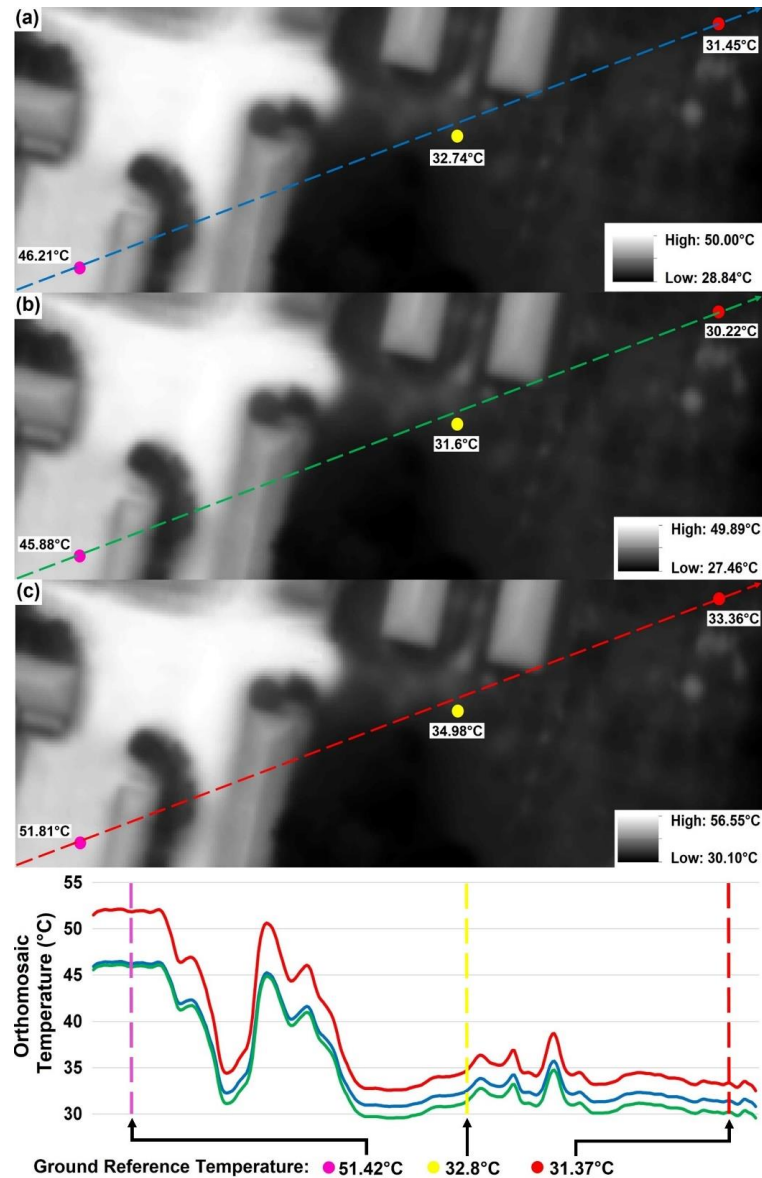


**Figure 9.** Zoomed view of the area based on orthomosaic from mission E, with temperature data calibrated with the factory (a), proximal (b), and general model (c). The profile graph illustrates temperature values along the transect from orthomosaics calibrated with the above-mentioned models. Dashed lines indicate where along the transect the reference targets (colored dots) are located.

## 2.4. Discussion

Considering that factory calibration of radiometric Lepton cameras is performed based on proximal analysis, using temperature readings of a blackbody radiator in a controlled environment (FLIR, 2018), we first reproduced this scenario to assess the performance of the sensor under ideal conditions and compared the results with a commercial camera. Under a stable ambient temperature and target ranging from 9.1 to 52.4 °C, the Lepton camera delivered accuracy within the values reported by the manufacturer, with an MAE of 1.45 °C and RMSE = 1.08 °C. These results were better than the values reported by Osroosh et al. (2018) during tests using radiometric Lepton sensors, in which an MAE of 2.1 °C and RMSE = 2.4 °C were obtained from a blackbody calibrator in a temperature range from 0 to 70 °C, conducted at a room temperature of 23 °C without replication. The lower

accuracy can be explained by the wider temperature range used during the tests but also the lack of a proper initial stabilization period required by uncooled thermal cameras to stabilize temperature readings (Berni et al., 2009; Smigaj et al., 2017; Kelly et al., 2019), which is not stated in the article. In comparison to the FLIR E5 camera, the accuracy of the Lepton camera readings was inferior, with residuals nearly double the E5 results (MAE = 0.48 °C, RMSE = 0.58 °C). Because E5 allows adjustments to perform calibration, optimizing temperature readings according to the informed air temperature, relative humidity, distance, and emissivity of the target, and thus more accurate results were expected. However, in terms of precision, the cameras yielded equivalent results, with  $R^2 > 0.99$ .

The camera performance on aerial mode was tested on different flight altitudes with replications throughout the day, aiming to provide a wide range of environmental and flying conditions to the analysis. We first assessed the effect of the distance between the camera and the target, which was based on three flight altitudes: 35, 65, and 100 m, using temperature data extracted from individual images without any processing and with the reference target positioned close to the central portion of the frame to avoid the vignetting effect. According to factory calibrated temperature data, the overall precision was similar among the flight altitudes tested ( $R^2 = 0.94 - 0.96$ ). The accuracy, however, decreased with the increase in flight altitude, with a higher variation between 35 and 65 m. Since TIR radiation is attenuated by the atmosphere (Berni et al., 2009; Meier et al., 2011; Hammerle et al., 2017), when increasing the distance between the camera from the target, less radiation will reach the sensor, resulting in lower temperature values and ultimately, weaker accuracy. This effect can be clearly observed on the overall regression models (Figure 4), in which the slope from the regression line elevates towards higher flight altitudes, demonstrating that the factory calibration gradually becomes more inaccurate as the distance between the camera and target is increased. In order to quantify the amount of radiation attenuated due to scattering and absorption by the atmospheric, radiative transfer models, such as MODTRAN (Berk et al., 1989; Berk et al., 1998; Berk et al., 2005; Berk et al., 2014), are often employed to correct TIR temperature, deriving profiles according to the distance between the camera and target object, relative humidity, and atmospheric temperature. The correction profiles' curves have a logarithmic shape when plotted against the distance between the camera and target (Sugiura et al., 2007), explaining the higher contrast of accuracy between the 35 and 65 m missions, and are significantly affected by relative humidity in low altitudes (Berni et al., 2009), justifying the distinct patterns of the coefficient values among regressions from missions conducted at different times of the day. Although radiative transfer models are considered efficient, implementing this calibration can become time-consuming for some users (Torres-Rua, 2017) and require input meteorological data, which is often not available.

Furthermore, other sources of error must be taken into account, especially the variations of the internal camera temperature experienced during flight conditions, which changes the sensitivity of the microbolometers, causing unstable temperature readings across time (Olbrycht et al., 2012; Budzier & Gerlach, 2015; Mestas-Carrascosa et al., 2018). A key strategy to mitigate the variations of the internal camera temperature is implementing a stabilization time needed for the camera to warm up before image acquisition (Berni et al., 2009; Smigaj et al., 2017; Kelly et al., 2019), associated with non-uniformity correction (NUC) being switched on to compensate the internal temperature drift effect and provide a harmonized response signal across the FPA sensor (Mestas-Carrascosa et al., 2018). The contrasting results reported from mission A, in which the 35 m mission delivered the worst performance among flights conducted in the early morning, were probably caused by an insufficient stabilization time before image acquisition. Even though the same warm-up time was used for all missions, the early morning flights experienced air temperature values approximately 10 °C lower than other missions, increasing the temperature difference between the initial and stabilized condition. This effect becomes evident when analyzing the performance

of subsequent missions from early morning (D and G), in which the camera's performance was significantly improved as a result of a steadier internal temperature. To avoid this issue, we recommend adding extra time for camera stabilization before flight campaigns, especially when the range between the air and internal camera temperature is more pronounced. Another effective measure is adding extra flight lines at the beginning of the mission to allow the camera temperature to stabilize according to the air temperature and wind conditions encountered during flight (Kelly et al., 2019).

Regarding the orthomosaic generation, the method developed to estimate camera positions was fundamental to overcome the alignment issues encountered with raw images, frequently reported in studies using the SfM algorithm in the mosaicking process of thermal images (Pech, 2013; Hoffmann et al., 2016; Dillen et al., 2016; Maes et al., 2017). In our study, performing the initial alignment process of raw images was even more difficult because the Lepton camera used did not record any coordinates for the images captured, and a post geo-tagging process was not feasible. The co-registration process based on enhanced contrast thermal images differs from other methods because it does not require additional images captured from a second camera (normally RGB) (Raza et al., 2014; Yahyanejad & Rinner, 2015; Maes et al., 2017), which is usually triggered simultaneously with the TIR sensor to allow the further co-registration process. As a result, the number of aligned images more than doubled and we were able to successfully align the raw images and generate the orthomosaics from eight out of nine missions. The only case we were not able to produce the orthomosaic was mission A, which experienced the aforementioned issues related to an insufficient warm-up time and dramatic changes in the temperature of target objects during the flight, which we believe affected the image alignment process. For this reason, missions from 35 m were not used during the blending modes and calibration analysis, maintaining only flight altitudes with complete replications to provide more reliable conclusions among the results.

The blending modes available in Agisoft Photoscan that were tested in our study resulted in orthomosaics with significant differences in terms of precision and accuracy, with contrasting visual aspects. When the orthomosaics are generated with the blending mode disabled, each resulting pixel is extracted from a single image with the view being closest to the nadir angle (Aasen & Bolten, 2018). On the other hand, when activated, the blending mode merges temperature data from different images, in which the average option combines the temperature values from all images covering the target object in a simple average (Perich et al., 2020), whereas the mosaic option applies a weighted average, with pixels closer to the nadir viewing angle being more important (Aragon et al., 2020). The results using the disabled mode provided the best overall results, with an  $R^2 = 0.96$  and RMSE of  $3.08\text{ }^\circ\text{C}$  ( $r\text{RMSE} = 9.74\%$ ), reflecting the benefit of using only close to nadir view images to reduce the vignette effect and avoiding the extra layer of uncertainty that blending modes might introduce as reported in other studies (Deery et al., 2016; Hoffmann et al., 2016). However, the visual result from orthomosaics obtained with the blending mode disabled (Figure 7c) can be an issue for applications aiming at the spatial distribution of TIR data, since the seamlines from the individual images used in the composition become apparent as a result of abrupt changes in temperature values from one image to another due to different viewing geometries (Perich et al., 2020). Results from the average blending mode were equivalent to the ones obtained with the disabled option, achieving the same overall precision ( $R^2 = 0.96$ ) and nearly the same accuracy, with an average RMSE of  $3.14\text{ }^\circ\text{C}$  ( $r\text{RMSE} = 9.93\%$ ). Since all overlapping images are combined in the average mode, using a wide range of camera positions and viewing angles to derive average temperature, a reduced level of accuracy is expected due to a more pronounced vignetting effect. The residuals, however, were equivalent to those obtained with the blending mode disabled, indicating that vignetting errors were not transferred to the orthomosaic generated with the average blending mode.

Similar results were obtained by Hoffmann et al. (2016), in which the orthomosaic produced with the average setting delivered results that were equivalent to the same orthomosaic generated excluding all images' edges, aiming to eliminate the vignetting effect. The final method tested was the mosaic option, which is the default blending mode in Agisoft, being constantly used to produce thermal orthomosaics (Ribeiro-Gomes et al., 2017; Kelly et al., 2019; Song & Park, 2020). Although it combines features from the average and disabled mode, the performance of this method was significantly lower, with an  $R^2 = 0.92$  and RMSE of  $3.93\text{ }^\circ\text{C}$  ( $r\text{RMSE} = 12.43\%$ ), indicating that this might not be the most appropriate blending mode to produce thermal orthomosaics. Considering that this method assigns a higher weight to close to nadir view images when averaging a pixel value, the expected accuracy would be close to the values obtained with the blending mode disabled. However, it is unclear if any other factors are taken into account and how exactly the software attributes the weight of each image to calculate the average value of each pixel. Other studies that employed the mosaic blending mode to produce thermal orthomosaics achieved results within the values observed in our study, with  $R^2$  ranging from 0.70 to 0.96 and RMSE between  $3.55$  and  $5.45\text{ }^\circ\text{C}$  (Ribeiro-Gomes et al., 2017; Kelly et al., 2019; Song & Park, 2020).

The results using the empirical line calibration demonstrated significant improvements in the camera performance for proximal and aerial conditions. When applying a proximal calibration model, the accuracy of the Lepton camera was significantly improved in relation to the factory configuration, reducing the MAE and RMSE in  $0.76$  and  $0.28\text{ }^\circ\text{C}$ , respectively. The achieved residuals are comparable to the ones obtained with the FLIR E5 camera, which accounts for optimizations for proximal readings, and corresponds with the accuracy reported by Osroosh et al. (2018) after calibrating FLIR Lepton sensors in laboratory conditions. However, when employed in aerial conditions, the proximal calibration model yielded results equivalent to the factory calibration, with the lowest accuracy among the models tested ( $\text{RMSE} = 3.40\text{ }^\circ\text{C}$ ), indicating that proximal approaches may not be suitable for aerial imaging. To be valid, proximal calibration should account for variations in the internal camera temperature, which are mainly influenced by ambient temperature (Sun et al., 2007; Nugent et al., 2013), and the images corrected for the attenuation of thermal radiance by the atmosphere.

On the other hand, calibration models based on the ground reference temperature consistently reduced the residuals from aerial missions, resulting in RMSE values between  $1.31$  and  $1.94\text{ }^\circ\text{C}$ . Since the models are adjusted combining TIR data with high-accuracy ground temperature, they can cover the main sources of error involved in aerial imagery, correcting the attenuation of radiation caused by the atmosphere, and reducing errors caused by variations in the camera temperature among different flights (Kelly et al., 2019). The general model, which combines datasets from flight altitudes of  $65$  and  $100\text{ m}$ , delivered the lowest residuals among the validation results, representing a reduction in MAE and RMSE values of  $1.19$  and  $1.83\text{ }^\circ\text{C}$ , respectively ( $\text{MAE} = 0.99\text{ }^\circ\text{C}$ ,  $\text{RMSE} = 1.31\text{ }^\circ\text{C}$ ). Other methods of calibration, such as the use of neural network calibration proposed by Ribeiro-Gomes et al. (2017), using sensor temperature and DN values as input variables, improved the accuracy of TIR measurements in  $2.18\text{ }^\circ\text{C}$ , with a final RMSE of  $1.37\text{ }^\circ\text{C}$ . Moreover, Mesas-Carrascosa et al. (2018) proposed a method to correct TIR temperature, removing the drift effect of microbolometer sensors based on the features used by SfM in the mosaicking process, and achieving a final accuracy within  $1\text{ }^\circ\text{C}$ . Using snow as the ground reference source, Pestana et al. (2019) corrected temperature derived from TIR imagery, increasing the accuracy by  $1\text{ }^\circ\text{C}$ . A similar approach was used by Gómez-Candón et al. (2016), in which thermal imagery was calibrated with a final accuracy of around  $1\text{ }^\circ\text{C}$  by using ground reference targets distributed across the flight path, deriving separate calibration models for images closest to each overpass. Furthermore, the results of specific models using individual datasets from the  $65$  and  $100\text{ m}$  missions, as well as datasets dividing missions according to the time of day, provided slightly higher

residuals, with RMSE values ranging from 1.32 to 1.94 °C. Even though the general model performed better in our tests, demonstrating that a more robust calibration might deliver better accuracies, the use of individual models generated from ground reference data acquired specifically for the flight campaign to be corrected ensures that any specific condition encountered will be properly covered in the calibration process, maintaining a reliable accuracy degree.

## 2.5. Conclusions

The low-cost Lepton camera tested in our study was able to deliver results within the specifications reported by the manufacturer, with accuracy values comparable to more expensive models in proximal and aerial conditions.

The aerial analysis focused on the use of orthomosaics to represent TIR data from UAV missions, in which the co-registering process proposed in our study was fundamental to overcome issues related to the use of non-geotagged images during the alignment process needed for orthomosaic obtention. Moreover, the blending modes tested significantly affected the overall accuracy of temperature derived from the orthomosaics, with the best results obtained with the average and disabled mode.

Although the accuracy decreased towards higher flight altitudes, demonstrating that the factory calibration does not account for atmospheric attenuation of TIR radiation, the precision remained stable among the flight altitudes tested, indicating that alternative calibration methods can be used to improve the final accuracy. Based on this assumption, calibration models were obtained relating camera DN to a high-accuracy reference temperature, reducing the error on TIR temperature readings by up to 1.83 °C, with a final accuracy below 2 °C.

## References

- Aasen H, Bolten, A (2018) Multi-temporal high-resolution imaging spectroscopy with hyperspectral 2D imagers—From theory to application. **Remote Sensing of Environment** 205:374-389
- Aragon B, Johansen K, Parkes S, Malbeteau Y, Al-Mashharawi S, Al-Amoudi T, Andrade CF, Turner D, Lucieer A, McCabe MF (2020) A calibration procedure for field and UAV-based uncooled thermal infrared instruments. **Sensors** 20:3316
- Aubrecht, DM, Helliker BR, Goulden ML, Roberts, DA, Still, CJ, Richardson, AD (2016) Continuous, long-term, high-frequency thermal imaging of vegetation: Uncertainties and recommended best practices. **Agricultural and Forest Meteorology** 228:315-326
- Baker EA, Lutz LK, McKenzie JM, Aubry-Wake C (2019) Improving the accuracy of time-lapse thermal infrared imaging for hydrologic applications. **Journal of Hydrology** 571:60–70
- Barsi JA, Barker JL, Schott JR (2003) An Atmospheric Correction Parameter Calculator For A Single Thermal Band Earth-Sensing Instrument. **Proceedings of IEEE International Geoscience and Remote Sensing Symposium** 3014-3016
- Berk A, Bernstein LS, Robertson DC (1989) MODTRAN: A Moderate Resolution Model for LOWTRAN7 (GL-TR-89-0122). **Air Force Geophysics Laboratory**

- Berk A, Bernstein LS, Anderson GP, Acharya PK, Robertson DC, Chetwynd JH, Adler-Golden SM (1998) MODTRAN cloud and multiple scattering upgrades with application to AVIRIS. **Remote Sensing of Environment** 65:367-375
- Berk A, Anderson GP, Acharya PK, Bernstein LS, Muratov L, Lee J, Fox M, Adler-Golden SM, Chetwynd JH, Hoke ML (2005) MODTRAN 5: A reformulated atmospheric band model with auxiliary species and practical multiple scattering options: Update. **Proceedings of SPIE - Algorithms and Technologies for Multispectral, Hyperspectral, and Ultraspectral Imagery XI** 5806:662-667
- Berk A, Conforti P, Kennett R, Perkins T, Hawes F, van den Bosch J (2014) MODTRAN6: A major upgrade of the MODTRAN radiative transfer code. **Proceedings of the 6th Workshop on Hyperspectral Image and Signal Processing: Evolution in Remote Sensing** 113-119
- Berni JAJ, Zarco-Tejada PJ, Suarez L, Fereres E (2009) Thermal and narrowband multispectral remote sensing for vegetation monitoring from an unmanned aerial vehicle. **IEEE Transactions on Geoscience and Remote Sensing** 47:722-738
- Buettner KJ, Kern CD (1965) The determination of infrared emissivities of terrestrial surfaces. **Journal of Geophysical Research** 70:1329-1337
- Budzier H, Gerlach G (2015) Calibration of uncooled thermal infrared cameras. **Journal of Sensors and Sensor Systems** 4:187-197
- Calderón R, Navas-Cortés JA, Lucena C, Zarco-Tejada PJ (2013) High-resolution airborne hyperspectral and thermal imagery for early detection of Verticillium wilt of olive using fluorescence, temperature and narrow-band spectral indices. **Remote Sensing of Environment** 139:231-245
- Colomina I, Molina P (2014) Unmanned aerial systems for photogrammetry and remote sensing: A review. **ISPRS Journal of Photogrammetry and Remote Sensing** 92:79-97
- Crusiol LGT, Nanni MR, Furlanetto RH, Sibaldelli RNR, Cezar E, Mertz-Henning LM, Nepomuceno AL, Neumaier N, Farias JRB (2020) UAV-based thermal imaging in the assessment of water status of soybean plants. **International Journal of Remote Sensing** 41:3243-3265
- Deery DM, Rebetzke GJ, Jimenez-Berni JA, James RA, Condon AG, Bovill WD, Hutchinson P, Scarrow J, Davy R, Furbank RT (2016) Methodology for high-throughput field phenotyping of canopy temperature using airborne thermography. **Frontiers in Plant Science** 7:1808
- Dillen M, Vanhellefont M, Verdonck P, Maes WH, Steppe K, Verheyen K (2016) Productivity, stand dynamics and the selection effect in a mixed willow clone short rotation coppice plantation. **Biomass Bioenergy** 87:46-54
- Eschbach D, Piasny G, Schmitt L, Pfister L, Grussenmeyer P, Koehl M, Skupinski G, Serradj A (2016) Thermal-infrared remote sensing of surface water-groundwater exchanges in a restored anastomosing channel (Upper Rhine River, France). **Hydrological Processes** 31:1113-1124
- Flasse SP, Ceccato P (1996) A contextual algorithm for AVHRR fire detection. **International Journal of Remote Sensing** 17:419-424
- FLIR (2018) FLIR Lepton: Engineering Datasheet. Available online: [www.flir.com/globalassets/imported-assets/document/flir-lepton-engineering-datasheet.pdf](http://www.flir.com/globalassets/imported-assets/document/flir-lepton-engineering-datasheet.pdf) (accessed on 12 December 2020)
- Gómez-Candón D, Virlet N, Labbé S, Jolivot A, Regnard JL (2016) Field phenotyping of water stress at tree scale by UAV-sensed imagery: New insights for thermal acquisition and calibration. **Precision Agriculture** 17:786-800

- Gonzalez-Dugo V, Zarco-Tejada P, Nicolás E, Nortes PA, Alarcón JJ, Intrigliolo DS, Fereres E (2013) Using high resolution UAV thermal imagery to assess the variability in the water status of five fruit tree species within a commercial orchard. **Precision Agriculture** 14:660-678
- Griggs M (1968) Emissivities of natural surfaces in the 8-to 14-micron spectral region. **Journal of Geophysical Research** 73:7545-7551
- Hammerle A, Meier F, Heigl M, Egger A, Leitinger G (2017) Implications of atmospheric conditions for analysis of surface temperature variability derived from landscape-scale thermography. **International Journal of Biometeorology** 61:575-588
- Hoffmann H, Nieto H, Jensen R, Guzinski R, Zarco-Tejada P, Friberg T (2016) Estimating evaporation with thermal UAV data and two-source energy balance models. **Hydrology and Earth System Sciences** 20:697-713
- Kay JE, Kampf SK, Handcock RN, Cherkauer KA, Gillespie AR, Burges SJ (2005) Accuracy of lake and stream temperatures estimated from thermal infrared images. **Journal of the American Water Resources Association** 41:1161-1175
- Kelly J, Kljun N, Olsson P-O, Mihai L, Liljeblad B, Weslien P, Klemedtsson L, Eklundh L (2019) Challenges and best practices for deriving temperature data from an uncalibrated UAV thermal infrared camera. **Remote Sensing** 11:567
- Khanal S, Fulton J, Shearer S (2017) An overview of current and potential applications of thermal remote sensing in precision agriculture. **Computers and Electronics in Agriculture** 139:22-32
- Klemas VV (2015) Coastal and environmental remote sensing from unmanned aerial vehicles: An overview. **Journal of Coastal Research** 31:1260-1267
- Kustas W, Anderson M (2009) Advances in thermal infrared remote sensing for land surface modeling. **Agricultural and Forest Meteorology** 149:2071-2081
- Maes WH, Huete AR, Steppe K (2017) Optimizing the processing of UAV-based thermal imagery. **Remote Sensing** 9:476
- Maimaitijiang M, Ghulam A, Sidike P, Hartling S, Maimaitiyiming M, Peterson K, Shavers E, Fishman J, Peterson J, Kadam S (2017) Unmanned Aerial System (UAS)-based phenotyping of soybean using multi-sensor data fusion and extreme learning machine. **ISPRS Journal of Photogrammetry and Remote Sensing** 134:43-58
- Martínez J, Egea G, Agüera J, Pérez-Ruiz M (2017) A cost-effective canopy temperature measurement system for precision agriculture: A case study on sugar beet. **Precision Agriculture** 18:95-110
- Matese A, Baraldi R, Berton A, Cesaraccio C, Di Gennaro SF, Duce P, Facini O, Mameli MG, Piga A, Zaldei A (2018) Estimation of Water Stress in grapevines using proximal and remote sensing methods. **Remote Sensing** 10:114
- Meier F, Scherer D, Richters J, Christen A (2011) Atmospheric correction of thermal-infrared imagery of the 3-d urban environment acquired in oblique viewing geometry. **Atmospheric Measurement Techniques** 4:909-922
- Mesas-Carrascosa FJ, Pérez-Porrás F, de Larriva JEM, Frau CM, Agüera-Vega F, Carvajal-Ramírez F, Martínez-Carricondo P, García-Ferrer A (2018) Drift correction of lightweight microbolometer thermal sensors on-board unmanned aerial vehicles. **Remote Sensing** 10:615
- Messina G, Modica G (2020) Applications of UAV thermal imagery in precision agriculture: State of the art and future research outlook. **Remote Sensing** 12:1491
- Mundy E, Gleeson T, Roberts M, Baraer M, McKenzie JM (2017) Thermal imagery of groundwater seeps: Possibilities and limitations. **Groundwater** 55:160-170

- Natarajan S, Basnayake J, Wei X, Lakshmanan P (2019) High-throughput phenotyping of indirect traits for early-stage selection in sugarcane breeding. **Remote Sensing** 11:2952
- Nugent PW, Shaw JA, Pust NJ (2013) Correcting for focal-plane-array temperature dependence in microbolometer infrared cameras lacking thermal stabilization. **Optical Engineering** 52:061304
- Olbrycht R, Wiecek B, De Mey G (2012) Thermal drift compensation method for microbolometer thermal cameras. **Applied Optics** 51:1788-1794
- Osroosh Y, Khot LR, Peters RT (2018) Economical thermal-RGB imaging system for monitoring agricultural crops. **Computers and Electronics in Agriculture** 147:34-43
- Pech K (2013) Generation of Multitemporal Thermal Orthophotos from UAV Data. **International Archives of the Photogrammetry, Remote Sensing and Spatial Information Sciences** 40:305-310
- Pestana S, Chickadel CC, Harpold A, Kostadinov TS, Pai H, Tyler S, Webster C, Lundquist JD (2019) Bias correction of airborne thermal infrared observations over forests using melting snow. **Water Resources Research** 55: 11331-11343
- Prakash A (2000) Thermal Remote Sensing: Concepts, Issues and Applications. **International Archives of Photogrammetry and Remote Sensing** 33:239-243
- Quintano C, Fernandez-Manso A, Roberts DA (2017) Burn severity mapping from Landsat MESMA fraction images and Land Surface Temperature. **Remote Sensing of Environment** 190:83-95
- R Core Team (2020) R: A Language and Environment for Statistical Computing. Available online: [www.rproject.org](http://www.rproject.org) (accessed on 17 December 2020).
- Raza S-e-A, Smith HK, Clarkson GJJ, Taylor G, Thompson AJ, Clarkson J, Rajpoot NM (2014) Automatic detection of regions in spinach canopies responding to soil moisture deficit using combined visible and thermal imagery. **PLoS ONE** 9:e9761
- Ribeiro-Gomes K, Hernández-López D, Ortega JF, Ballesteros R, Poblete T, Moreno MA (2017) Uncooled thermal camera calibration and optimization of the photogrammetry process for UAV applications in agriculture. **Sensors** 17:2173
- Ritter M (2020) Further Development of an Open-Source Thermal Imaging System in Terms of Hardware, Software and Performance Optimizations. Available online: [www.github.com/maxritter/DIY-Thermocam](https://www.github.com/maxritter/DIY-Thermocam) (accessed on 12 December 2020)
- Santesteban LG, Di Gennaro SF, Herrero-Langreo A, Miranda C, Royo JB, Matese A (2017) High-resolution UAV-based thermal imaging to estimate the instantaneous and seasonal variability of plant water status within a vineyard. **Agricultural Water Management** 183:49-59
- Smigaj M, Gaulton R, Barr SL, Suarez JC (2016) Investigating the performance of a low-cost thermal imager for forestry applications. **Proceedings of SPIE: Image and Signal Processing for Remote Sensing XXII** 100041E
- Smigaj M, Gaulton R, Suarez JC, Barr SL (2017) Use of miniature thermal cameras for detection of physiological stress in conifers. **Remote Sensing** 9:957
- Song B, Park K (2020) Verification of accuracy of unmanned aerial vehicle (UAV) land surface temperature images using in-situ data. **Remote Sensing** 12:288
- Sugiura R, Noguchi N, Ishii K (2007) Correction of low-altitude thermal images applied to estimating soil water status. **Biosystems Engineering** 96:301-313

- Sun L, Chang B, Zhang J, Qiu Y, Qian Y, Tian S (2007) Analysis and measurement of thermal-electrical performance of microbolometer detector. **Proceedings of SPIE: Optoelectronic Materials and Devices II** 678231
- Torres-Rua A (2017) Vicarious calibration of sUAS microbolometer temperature imagery for estimation of radiometric land surface temperature. **Sensors** 17:1499
- Verhoeven G (2011) Taking computer vision aloft - Archaeological three-dimensional reconstructions from aerial photographs with photoscan. **Archaeological Prospection** 18:67-73
- Yahyanejad S, Rinner B (2015) A fast and mobile system for registration of low-altitude visual and thermal aerial images using multiple small-scale UAVs. **ISPRS Journal of Photogrammetry and Remote Sensing** 104:189-202
- Zhang L, Niu Y, Zhang H, Han W, Li G, Tang J, Peng X (2019) Maize canopy temperature extracted from UAV thermal and RGB imagery and its application in water stress monitoring. **Frontiers in Plant Sciences** 10:1-18



### 3. PREDICTING SOIL WATER CONTENT AND MAIZE WATER STRESS THROUGH CANOPY TEMPERATURE IMAGERY

#### ABSTRACT

Restrictions on soil water supply can dramatically reduce crop yields by affecting the growth and development of plants. For this reason, screening tools that can early detect crop water stress has been long investigated, with canopy temperature (CT) being widely used for this purpose. In this study, we investigated the relationship between canopy temperature retrieved from unmanned aerial vehicle (UAV) based thermal imagery with soil and plant attributes related to soil-plant water dynamic, using a rainfed maize field as the area of study. The flight mission was conducted on late vegetative stage and at solar noon, when a considerable soil water deficit was detected according to the soil water balance model used. While the images were being taken, a guided sampling was conducted to determine soil and plant water content across the field. The sampling results demonstrated the spatial variability of soil water status, with soil water storage (SWS) presenting 23.3 % of variation and values close to the permanent wilting point (PWP), reflecting CT readings that ranged from 32.8 to 40.6 °C among the sampling locations. Although CT correlated well with most of the soil physical attributes related to water dynamic, the simple linear regression between CT and soil water content variables yielded coefficients of determination ( $R^2$ )  $\leq 0.26$ , indicating that CT alone is not sufficient to predict soil water status. Nonetheless, when CT was combined with some soil physical attributes in a stepwise multiple linear regression the prediction capacity was significantly increased achieving  $R^2$  values  $\geq 0.83$ . Moreover, the variables related to plant water status presented similar results, with plant water content presenting  $R^2$  values  $\leq 0.25$  in simple linear regression models. However, since the plant water status variables used in the study potentially represent long-term water stress, it seems feasible carrying more studies to confirm these results, preferably using plant variables that match the onset drought stress detected through thermal data.

**Keywords:** UAV, thermography, thermal camera, crop water stress

#### 3.1. Introduction

Drought stress is considered the most damaging of all abiotic stresses, limiting the growth and development of plants and ultimately their yield (Lambers et al., 2008; Gautan & Pagay, 2020). Climate change is expected to intensify the incidence of extreme weather events including droughts spells (Fedoroff et al., 2010), which will demand optimization of agricultural practices that can maximize water use efficiency to sustain the actual crop yields even under rainfed conditions. Precision agriculture (PA) consists of a site-specific form of agriculture that focuses on optimizing farm inputs by doing the right management practice at the right place, right time and appropriate intensity (Gebbers & Adamchuk, 2010; Mulla, 2013; Maes & Steppe, 2019). To implement this concept, a proper characterization of within-field spatial variability is essential to understand the potential limiting factors.

Because soil physical attributes often present moderate to high spatial variability (Mulla & McBratney, 2001), the amount of water available for plants tends to vary across the field as function of the soil water holding capacity (SWHC) (Heiskanen & Makitalo, 2002; Sobieraj et al., 2003; Iqbal et al., 2005). When soil water becomes limiting the plants respond promptly by regulating the stomatal conductance to reduce transpiration as a water-saving strategy, which leads to a lower evaporative cooling while increasing leaf temperature (Idso et al., 1981 Jones,

2004; Gago et al., 2015). For this reason, canopy temperature has long been used as a proxy to assess crop water status (Jackson et al., 1981), with remotely sensed temperature being constantly used for this purpose. Therefore, many studies have successfully used thermal cameras retrieving canopy temperature to assess plant water stress in crops like maize (Zhang et al., 2019), soybeans (Crusiol et al., 2020), cotton (Bian et al., 2019), pinto beans (Zhou et al., 2018), citrus orchards (Zarco-Tejada et al., 2012) and grapevines (Bellvert et al., 2014; Matese et al., 2018).

Most of these studies reflect technology advances with the development of cost-effective miniaturized thermal cameras that occurred during the last 20 years (Berni et al., 2009; Klemas, 2015; Aubrecht et al., 2016), which are lightweight and low power enough to fit onto unmanned aerial vehicle (UAV) platforms (Kelly et al., 2019). From aerial thermal imagery, crop canopy temperature can be monitored with high temporal and spatial resolution at field scale, representing a rapid response tool to detect and quantify plant water stress (Gago et al., 2015; Radoglou-Grammatikis et al., 2020). Although plant water stress expresses restrictions in soil water storage, most studies focus on investigating the relationship between canopy temperature with physiological water stress indicators, such as leaf water potential and stomatal conductance, aiming to validate prediction models for onset plant water stress, with very few studies exploring how soil water content influence these measurements. In addition, thermal data has been widely employed as an irrigation resource management tool, with rare studies assessing its use on rainfed crops, particularly rainfed maize, where no studies using UAV-based thermal imagery as a plant water stress indicator have been yet reported.

Therefore, the objective of this study was to explore the use of UAV thermal imagery for monitoring the spatial variability of maize water stress on a rainfed field. The relationship between remotely sensed canopy temperature and maize water stress was assessed based on plant and soil attributes sampled across the area of study, focusing on direct measurements of soil and plant water content along with crop yield components and soil physical attributes.

## 3.2. Materials and Methods

### 3.2.1. Study area

The study was conducted in a 40.1 ha field located in Itararé, São Paulo state, southern Brazil (24°01'36.93" S - 49°25'33.46" W, 640 m of altitude). The local climate is defined according to Köppen classification as subtropical humid (Cfa) (Alvares et al., 2013). Most rainfall occurs between October and March, with a relatively dry period between April and August. The annual average rainfall is 1532 mm, with mean temperature of 17 °C (Tremocoldi & Brunini, 2008). The main soil type in the region is a Dystrophic Red-Yellow Oxisol (Rossi, 2017), with a sandy clay loam texture. The terrain slope average is 11 %, which requires its cultivation in contours and the use of terraces.

The crop evaluated in the study was maize sown on February 18th, 2019 as a second crop with the variety MS30A37PW, rows spaced in 0.45 m and final plant population of 63,000 plants ha<sup>-1</sup>. The area has a long historic under no-tillage system, being cultivated in a rainfed condition with a soybean-maize rotation system during the summer cropping seasons, and with wheat (*Triticum* spp.) or black oat (*Avena strigosa* Schreb.) during the winter season.

### 3.2.2. Guided sampling

In order to capture the spatial variability of yield-limiting factors through sampling, we first divided the field into homogeneous zones and then distributed the samples accordingly. These zones were generated using pre-existing data from georeferenced grid soil sampling, and vegetation indices obtained with active canopy sensors from previous cropping seasons.

To obtain the homogeneous zones, we first generated surface maps from each soil attribute and vegetation index using ordinary kriging. Experimental semi-variograms were built for every variable using VESPER 1.6 software (Minasny et al., 2006), in which the semi-variogram model that provided the lowest residuals was selected to produce the surface map. Furthermore, a Pearson correlation matrix was calculated using the interpolated maps, selecting only soil attributes and vegetation index maps that presented a  $p$ -value  $\leq 0.05$  in the  $t$  test to compose the further analysis.

To delineate the zones, a clustering analysis was performed using the fuzzy  $c$ -means algorithm featured in the MZA software (Fridgen et al., 2004). The selected variables were merged into a single text table and imported by the MZA software, setting the Euclidian as distance criteria, fuzziness exponent set as 1.2, and the number of iterations limited to 300. The optimal number of zones (clusters) was defined based on the Fuzziness Performance Index (FPI) and the Normalized Classification Entropy (NCE), choosing the number of clusters that yielded the lowest values for both FPI and NCE (Odeh et al., 1992; Fridgen et al., 2000). Based on the clusters obtained, five sampling points were randomly distributed within each zone to guide further sampling procedures.

### 3.2.3. UAV thermal imagery

Since the main goal of this study was to assess the ability of thermal imagery in detecting crop water stress, one of the key points was detecting a suitable time during the growing season to collect thermal images. For this reason, we constantly monitored the weather conditions and implemented a soil water balance model to identify periods with water deficiency that would prompt the aerial mission. Other restrictive factors imposed were to conduct aerial missions only after canopy closure over the interrow, avoiding soil background effect on TIR images, and before senescence, in which the water consumption is not significant. Based on these assumptions, a single aerial mission was conducted on April 2nd, 2019, when maize was at a V12 growth stage with canopy completely closed, and with a soil water deficiency of 4.1 mm according to an estimated 10-day serial water balance (Thornthwaite and Mather, 1955) using gridded database provided by the National Aeronautics and Space Administration/Prediction of World Wide Energy Resources (NASA/POWER) (Figure 1).

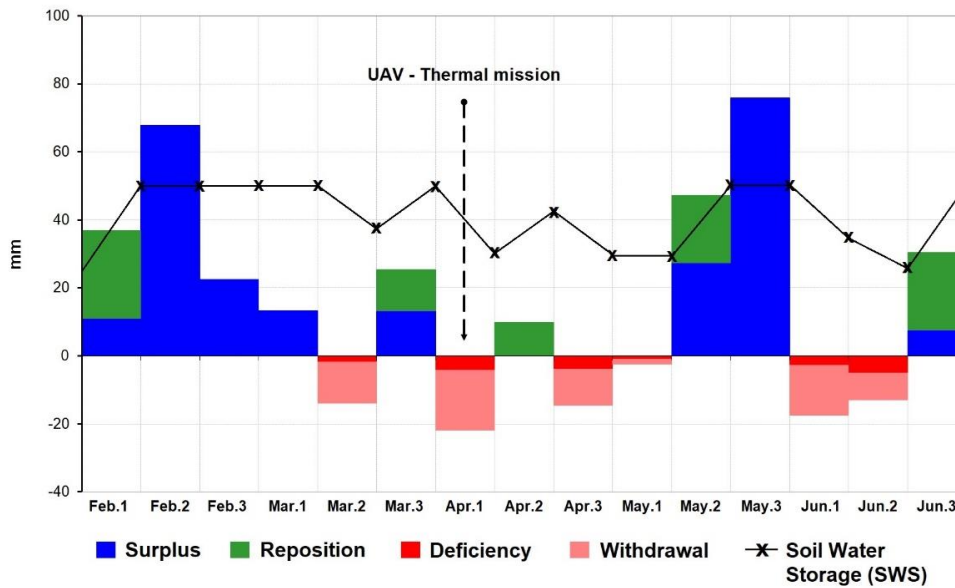


**Figure 1.** Climatological water balance (Thornthwaite & Mather, 1955) calculated in a ten-day time step and considering 50 mm of soil water holding capacity.

The flight mission was conducted around two hours past solar noon (between 13:38 and 14:31 local time), which is considered the optimal time to evaluate plant water stress (Alchanatis et al., 2010; Lu et al., 1998). There were no clouds during the flight, with mean air temperature of 30.5 °C, relative humidity of 55 %, vapour pressure deficit (VPD) of 1.96 kPa (Anderson, 1936) and wind speeds up to 2.5 ms<sup>-1</sup>, according to a nearby weather station.

A low-cost radiometric calibrated FLIR Lepton 3.5 thermal camera (FLIR Systems, Inc., Wilsonville, OR, USA) was used to obtain the aerial images. The camera is composed of an uncooled VOx microbolometer FPA, with a spectral range of 8-14 µm and resolution of 160 x 120 pixels. Temperature readings are extracted from 14-bit images with a resolution of 0.05 °C and absolute measurement accuracy of ± 5 °C or 5 % over a range between -10°C and 140 °C. The camera was attached to a DJI Phantom 4 quadcopter (SZ DJI Technology Co., Shenzhen, China) and adjusted to collect close to nadir images, being powered up 15 minutes before flight to ensure a proper stabilization time (Kelly et al., 2019). In the flight planning, parameters were adjusted to deliver images with forward and side overlap of ≥ 75% and ≥ 60%, respectively, at 100 m above ground level.

The image processing necessary to generate the thermal orthomosaic was implemented following the methodology described by Acorsi, Martello and Gimenez (2020), using the Agisoft Photoscan Professional (v. 1.2.6, Agisoft LLC, St. Petersburg, Russia) to build the orthomosaic. For georeferencing purposes, a total of six ground control points (GCPs) were previously located in the field using distinguishable targets, with their coordinates measured following a post-processing kinematic (PPK) method, using a pair of single-frequency global navigation satellite system (GNSS) receivers (GTR-ABT TechGeo, Brazil).

Once the orthomosaic was finished, it was imported to ArcGIS software (v. 10.2.2, ESRI Ltd., Redlands, CA, USA) along with the waypoints corresponding to the sampling locations defined in 2.2.2. Circular buffers of 3 m radius were generated using the sampling location coordinates, which were then used to extract average temperature values from the thermal orthomosaic for each point.

### 3.2.4. Field data

To investigate the relationship between remotely sensed canopy temperature (CT) and plant water status, we explored attributes that could explain the dynamic of water in both soil and plant. In this sense, many physical attributes from soil were assessed as well as some chemical properties that can influence its capacity in retaining water. On the other hand, we also analyzed plant variables reflecting their water status along with productivity indicators that can express drought stress.

#### 3.2.4.1. Soil attributes

On the same day the aerial mission was carried out, soil samples were collected in the 0 – 0.2 m depth on every pre-defined sampling location, samples were composed of five sub-samples distributed within a three-meter radius. The samples were sealed in plastic bags and taken to a laboratory for further analysis. To determine the gravimetric water content (SGWC), the samples were first weighed and then oven dried at 105 °C for 48 hours and re-weighed to measure the water content lost. Moreover, granulometry and chemical characterization (Fine Sand; Coarse Sand; Clay; Silt; pH; P; K; Ca; Mg; H+Al; Organic Matter; Sum of Bases; Cation Exchange Capacity and Base Saturation) was performed according to Teixeira et al. (2017).

After the crop was harvested, undisturbed soil samples were also taken at each sampling point, from trenches at 0.12 and 0.35 m depths, with two replications, collected using metal rings with a dimension of 0.05 x 0.05 m (diameter x height). In the laboratory, the samples were saturated and then weighed. Moreover, the samples were transferred and kept on a tension table with a – 6 kPa water potential until mass stabilization and then re-weighed. Lastly, the samples were oven dried at 105 °C for 48 h and weighed once more. Thus, the macroporosity (MaP) was determined by the mass difference between saturated samples and samples submitted to the – 6 kPa water potential, whereas the microporosity (MiP) was obtained from the mass difference between samples at -6 kPa water potential and oven dried samples (Teixeira et al., 2017). In addition, the bulk density (BD) was also determined, dividing the dry mass of soil by the volume of the metal ring. The BD information was then used to calculate the soil volumetric water content (SVWC), multiplying the gravimetric water content by BD (Dirksen, 1999).

Along with the undisturbed soil sampling, the soil resistance to penetration (SRP) was also measured in the field, within 0 – 0.40 m depth, using a handheld digital penetrometer (PLG1020, Falker, Porto Alegre, Brazil). The average SRP values were extracted from 10 sub-samples measured within a three-meter radius of every sampling location, positioned between the previous crop rows, with soil moisture content close to field capacity.

The soil water holding capacity (SWHC) was calculated according to the model proposed by Van Genuchten (1980), using water retention parameters derived from a pedotransfer function (level 3) proposed by Tomasella, Hodnett and Rossato (2000). The input variables used were the soil texture, organic carbon and bulk density (at 0.12 m depth), with the soil volumetric water content difference between – 10 kPa and -1.500 kPa water potentials used to represent the SWHC on a 0 - 0.4 m soil depth. With the SWHC obtained for each sampling point, a 10-day climatological water balance based on the Thornthwaite and Matter (1955) model was implemented using daily gridded NASA/POWER database as input meteorological variables, which allowed the estimation of the soil water storage (SWC) when the aerial mission was conducted.

### 3.2.4.2. Plant attributes

To quantify the amount of water present in the plants and compare it with CT readings, a destructive biomass sampling was carried out when aerial images were obtained. The process consisted of determining the plant population at each sampling location, by counting the number of plants of four 20 m length rows. Among the counted plants, 10 individuals were randomly selected and cut at the soil surface to be immediately weighed using a portable digital balance. Two of these plants were re-weighed and then packed in paper bags to be oven dried at 65 °C until a constant weight mass was achieved. The fresh biomass (FBM) was obtained by multiplying the plant average weight measured in the field by the plant population, while the dry biomass (DBM) was determined using the oven dried weight also multiplied by plant population. The amount of water lost during the drying process was used as a proxy to assess the plant water status, being represented by two variables: the biomass water content (BWC) and biomass relative water content (BRWC). The BWC represents the absolute mass of water present in the biomass per area, as the difference between FBM by DBM. On the other hand, BRWC specifies the relative mass of water in percentage values, dividing the BWC by FBM and then multiplying by 100 (Elsayed et al., 2017).

When the crop reached physiological maturity (July 7th), two rows with 10 meters each were manually harvested to measure yield components at every sampling location. The yield components were determined based on all ears harvested, including the average number of ears per plant (ER); rows per ear (RE); kernels per row (KR); ear length (EL); ear diameter (ED) and ear weight (EW). Moreover, the ears were threshed and the grains oven dried at 65 °C for 48 h to calculate and correct the grain yield (YLD) for a 13% grain moisture.

### 3.2.4.3. Statistical analysis

Datasets from soil and plant, including CT were analyzed using the R software (R Development Core Team, 2020), starting with descriptive statistics, calculating the mean, minimum (Min) and maximum (Max) values, standard deviation (SD), coefficient of variation (CV), and also the skewness and kurtosis values. Furthermore, the normality of the data was checked by Shapiro-Wilk's test at 5 % of significance, when necessary, a Box-Cox transformation was applied to achieve homoscedasticity.

To understand the multiple relationships among the variables, an exploratory principal component analysis (PCA) was applied, dividing the dataset into plant and soil variables, with CT included in both cases. According to the results, some variables were then grouped to reduce the multicollinearity, and each of these groups was submitted to a second PCA excluding independent variables (CT; SWS; SVWC; BWC; BRWC) and maintaining the first division of soil and plant attributes. The suitability of the data for each PCA was evaluated using the Bartlett's sphericity test at 0.05 significance level, and with the Kayser-Meyer-Olkin (KMO) test, admitting values  $\geq 0.5$ . If a lower KMO value was observed, the variable with the lowest score in the measure of sampling adequacy (MSA) would be removed from the analysis, repeating this process until reaching at least 0.5 in the KMO test. Finally, the remaining dataset was transformed into non-correlated variables named principal components (PCs), selected according to Kaiser's criterion (eigenvalues  $> 1$ ).

The relationship between the obtained PCs with other variables was first investigated using a Pearson correlation matrix, including variables classified as independent and other attributes not included in the principal component analysis. Moreover, simple linear regression models were built relating CT with variables that represent the amount of water present in the soil (SVWC and SWS) and in the plants (BWC and BRWC). To better understand

how CT can contribute explaining water status, other variables that are linked to water dynamics in soil and plant were combined with CT as independent variables in multiple linear regressions followed by a stepwise procedure to select the best predictors at a significance level of 5 % (F-test). Additionally, we also tested which variables of soil and plant interact with CT by employing the same stepwise multiple linear regression model using CT as the dependent variable, with all the regression models residuals tested for normality by Shapiro Wilk's test at 5 % of significance.

### 3.3. Results

The clustering analysis used to delineate the homogeneous zones resulted in four regions, with FPI and NCE values of 0.21 and 0.13, respectively. The input variables selected to perform the clustering included soil organic matter (OM) and potential cation exchange capacity (CEC) maps, in addition to normalized difference vegetation index (NDVI) and normalized difference red edge (NDRE) maps of wheat crop from 2012/2015 and 2016/2018 growing seasons, respectively. Five sampling points were then located within each zone, placed between the terraces of the field (Figure 2b).

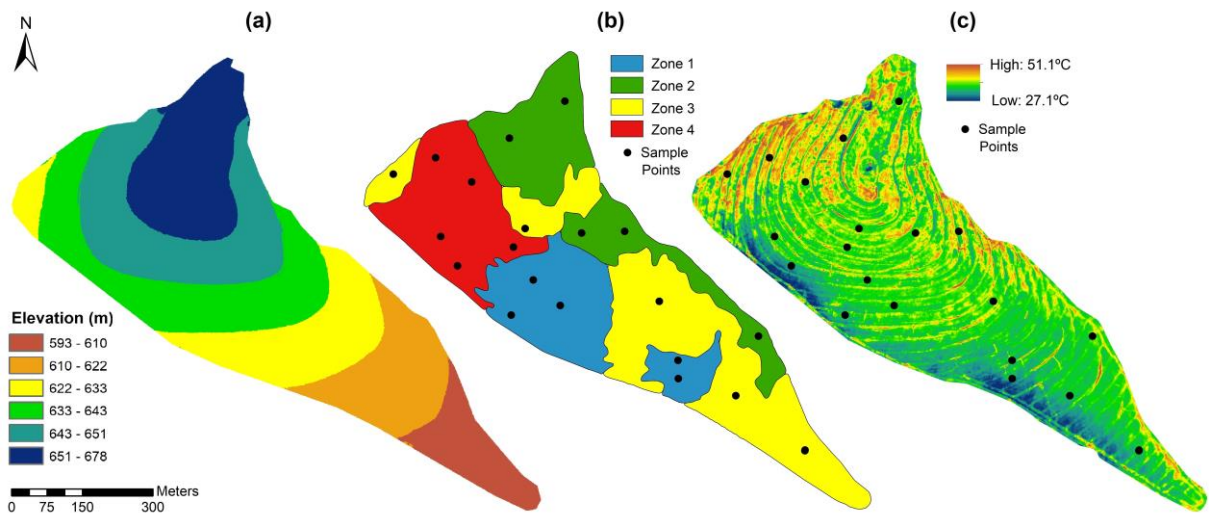


**Figure 2.** Hypsometric map of the experimental field (a) with the homogeneous zones and sampling locations (b), and the thermal orthomosaic (c).

The soil and plant attributes sampled in the study generated a total of 42 variables, which are listed in Table 1, including the descriptive statistics results. The CT readings from the 20 sampling locations were extracted from the thermal orthomosaic generated (Figure 2c), which presented a spatial resolution of  $0.63 \text{ m pixel}^{-1}$ . The results showed that CT ranged from 32.81 to 40.58 °C among the sampling points, whereas some attributes from soil water status, like SVWC and SWS varied between 0.13 and 0.22  $\text{m}^3 \text{ m}^{-3}$ , and from 21.93 to 59.76 mm, respectively. Regarding plant water content, BRWC values between 83.14 and 91.03% were observed, with BWC ranging from 15.24 to 32.12  $\text{Mg ha}^{-1}$ .

**Table 1.** Descriptive statistics of the soil and plant attributes extracted from the sampling locations.

| Variables   | Abbrev                   | n   | Mean  | Min   | Max   | SD    | CV (%) | Skew  | Kurt  |
|---|--------------------------|-----|-------|-------|-------|-------|--------|-------|-------|
| Fine Sand (%)   | <b>FS</b>                | 20  | 41.81 | 33.10 | 51.90 | 4.71  | 11.28  | -0.14 | 0.13  |
| Coarse Sand (%)   | <b>CS</b>                | 20  | 13.32 | 10.80 | 16.50 | 1.66  | 12.49  | 0.60  | -0.63 |
| Clay (%)  | <b>C</b>                 | 20  | 28.45 | 19.70 | 37.30 | 5.17  | 18.18  | 0.17  | -0.33 |
| Silt  | <b>S</b>                 | 20  | 16.42 | 7.80  | 29.60 | 5.60  | 34.12  | 0.50  | 0.23  |
| pH  | -                        | 20  | 4.76  | 4.50  | 5.40  | 0.20  | 4.12   | 1.97  | 5.51  |
| Organic Matter (%)  | <b>OM</b>                | 20  | 2.68  | 1.90  | 4.20  | 0.48  | 17.94  | 1.61  | 4.59  |
| P (mg dm <sup>-3</sup> )  | -                        | 20  | 44.10 | 24.00 | 72.00 | 11.14 | 25.27  | 0.63  | 0.99  |
| K (mmolc dm <sup>-3</sup> )                                     | -                        | 20  | 1.89  | 0.90  | 3.70  | 0.69  | 36.60  | 0.89  | 1.11  |
| Ca (mmolc dm <sup>-3</sup> )                                    | -                        | 20  | 27.65 | 16.00 | 50.00 | 7.07  | 25.58  | 1.72  | 4.58  |
| Mg (mmolc dm <sup>-3</sup> )                                    | -                        | 20  | 12.35 | 7.00  | 23.00 | 4.00  | 32.42  | 1.45  | 2.21  |
| H+Al (mmolc dm <sup>-3</sup> )                                  | -                        | 20  | 43.40 | 31.00 | 64.00 | 7.84  | 18.06  | 0.88  | 1.13  |
| Potential Cation Exchange Capacity (mmolc dm <sup>-3</sup> )    | <b>CEC</b>               | 20  | 85.28 | 63.00 | 105.9 | 11.09 | 13.01  | 0.13  | -0.21 |
| Base Saturation (%)   | <b>BS</b>                | 20  | 48.75 | 38.00 | 71.00 | 7.91  | 16.22  | 1.40  | 2.38  |
| Microporosity <sup>1</sup> (m <sup>3</sup> m <sup>-3</sup> )    | <b>MiP<sup>1</sup></b>   | 40  | 0.29  | 0.26  | 0.34  | 0.02  | 8.25   | 0.67  | -0.37 |
| Macroporosity <sup>1</sup> (m <sup>3</sup> m <sup>-3</sup> )    | <b>MaP<sup>1</sup></b>   | 40  | 0.05  | 0.03  | 0.08  | 0.01  | 23.97  | 0.76  | 1.31  |
| Bulk Density <sup>1</sup> (Mg m <sup>-3</sup> )                 | <b>BD<sup>1</sup></b>    | 40  | 1.53  | 1.33  | 1.67  | 0.09  | 5.78   | -0.53 | -0.17 |
| Microporosity <sup>2</sup> (m <sup>3</sup> m <sup>-3</sup> )    | <b>MiP<sup>2</sup></b>   | 40  | 0.34  | 0.29  | 0.38  | 0.02  | 7.03   | -0.26 | -0.60 |
| Macroporosity <sup>2</sup> (m <sup>3</sup> m <sup>-3</sup> )    | <b>MaP<sup>2</sup></b>   | 40  | 0.06  | 0.03  | 0.11  | 0.02  | 31.24  | 0.57  | -0.09 |
| Bulk Density <sup>2</sup> (Mg m <sup>-3</sup> )                 | <b>BD<sup>2</sup></b>    | 40  | 1.37  | 1.19  | 1.59  | 0.09  | 6.92   | 0.34  | 0.70  |
| Soil Resistance to Penetration at 0.05 m (MPa)                  | <b>SRP<sub>.05</sub></b> | 200 | 0.43  | 0.10  | 0.91  | 0.20  | 0.05   | 0.43  | 0.27  |
| Soil Resistance to Penetration at 0.10 m (MPa)                  | <b>SRP<sub>.10</sub></b> | 200 | 1.59  | 1.05  | 2.49  | 0.39  | 0.02   | 0.55  | -0.03 |
| Soil Resistance to Penetration at 0.15 m (MPa)                  | <b>SRP<sub>.15</sub></b> | 200 | 2.12  | 1.59  | 2.62  | 0.35  | 0.02   | 0.12  | -1.51 |
| Soil Resistance to Penetration at 0.20 m (MPa)                  | <b>SRP<sub>.20</sub></b> | 200 | 2.33  | 1.77  | 2.93  | 0.29  | 0.01   | 0.51  | 0.18  |
| Soil Resistance to Penetration at 0.25 m (MPa)                  | <b>SRP<sub>.25</sub></b> | 200 | 2.11  | 1.68  | 3.06  | 0.35  | 0.02   | 1.14  | 1.62  |
| Soil Resistance to Penetration at 0.30 m (MPa)                  | <b>SRP<sub>.30</sub></b> | 200 | 1.89  | 1.42  | 2.43  | 0.29  | 0.02   | 0.78  | -0.29 |
| Soil Resistance to Penetration at 0.35 m (MPa)                  | <b>SRP<sub>.35</sub></b> | 200 | 1.77  | 1.50  | 2.54  | 0.24  | 0.01   | 2.00  | 5.19  |
| Soil Resistance to Penetration at 0.40 m (MPa)                  | <b>SRP<sub>.40</sub></b> | 200 | 1.72  | 1.34  | 2.73  | 0.31  | 0.02   | 1.94  | 4.77  |
| Soil Volumetric Water Content (m <sup>3</sup> m <sup>-3</sup> ) | <b>SVWC</b>              | 20  | 0.18  | 0.13  | 0.22  | 0.02  | 12.69  | -0.23 | -0.42 |
| Soil Water Holding Capacity (mm)                                | <b>SWHC</b>              | 20  | 49.91 | 33.30 | 72.41 | 9.16  | 18.35  | 0.51  | 0.85  |
| Soil Water Storage (mm)   | <b>SWS</b>               | 20  | 37.78 | 21.93 | 59.76 | 8.83  | 23.36  | 0.55  | 0.95  |
| Biomass Relative Water Content (%)                              | <b>BRWC</b>              | 20  | 87.14 | 83.14 | 91.03 | 1.84  | 2.11   | -0.11 | 0.08  |
| Biomass Water Content (Mg ha <sup>-1</sup> )                    | <b>BWC</b>               | 20  | 26.23 | 15.24 | 32.12 | 4.92  | 18.76  | -0.82 | 0.10  |
| Fresh Biomass (Mg ha <sup>-1</sup> )                            | <b>FBM</b>               | 20  | 30.03 | 17.80 | 36.54 | 5.28  | 17.57  | -1.02 | 0.89  |
| Dry Biomass (Mg ha <sup>-1</sup> )                              | <b>DBM</b>               | 20  | 3.81  | 2.55  | 4.78  | 0.60  | 15.76  | -0.44 | -0.26 |
| Grain Yield (Mg ha <sup>-1</sup> )                              | <b>YLD</b>               | 20  | 9.15  | 6.98  | 11.45 | 1.21  | 13.26  | -0.19 | -0.61 |
| Ears per Plant  | <b>EP</b>                | 20  | 1.00  | 0.84  | 1.15  | 0.08  | 8.34   | 0.13  | -0.31 |
| Rows per Ear  | <b>RE</b>                | 20  | 15.29 | 14.93 | 15.48 | 0.15  | 0.95   | -0.78 | 0.53  |
| Kernels per Row   | <b>KR</b>                | 20  | 30.47 | 26.82 | 33.59 | 1.79  | 5.89   | -0.37 | -0.07 |
| Ear Length (cm)   | <b>EL</b>                | 20  | 15.68 | 14.53 | 16.51 | 0.61  | 3.91   | -0.79 | -0.31 |
| Ear Diameter (cm)   | <b>ED</b>                | 20  | 16.82 | 16.23 | 17.37 | 0.29  | 1.71   | -0.13 | -0.39 |
| Ear weight (g)  | <b>EW</b>                | 20  | 235.7 | 189.9 | 274.6 | 23.28 | 9.88   | -0.51 | -0.47 |
| Canopy Temperature (°C)   | <b>CT</b>                | 20  | 35.89 | 32.81 | 40.58 | 2.00  | 5.57   | 0.65  | 0.53  |

Abbrev.: abbreviation; n.: number of samples; Min.: minimum value observed; Max.: maximum value observed; SD.: standard deviation; CV.: coefficient of variation; Skew.: skewness; Kurt.: kurtosis; <sup>1</sup>0.15 m soil depth; <sup>2</sup>0.35 m soil depth.

The exploratory PCA confirmed the multicollinearity among soil and plant datasets as shown in the loading plots of Figure 3. Because the soil dataset includes a greater number of variables, mostly related to soil physical attributes, the multicollinearity was more evident, with variables extracted from undisturbed soil samples (MiP, MaP and BS) and SRP measurements presenting similar behaviors (Figure 3a). The same characteristic was observed with soil chemical attributes and yield components (Figure 3b), demonstrating that these variables could be grouped and then converted to PCs using a second PCA, simplifying further analysis and interpretation through a smaller number of variables.

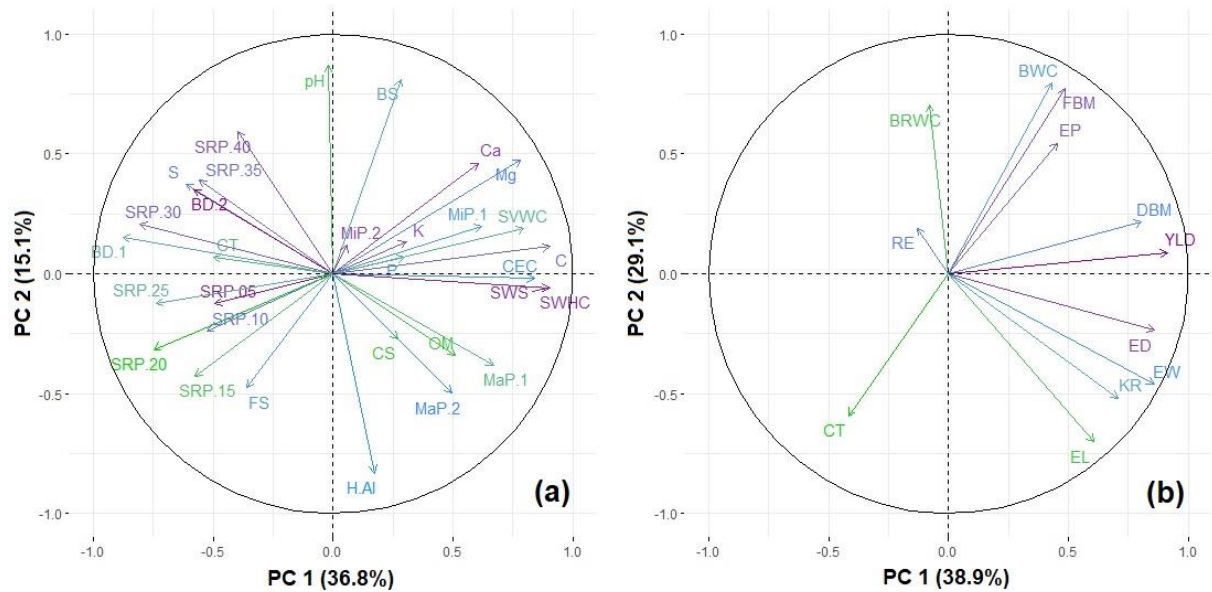


**Figure 3.** Biplots of the loadings from the exploratory PCA obtained with soil (a) and plant variables (b).

The first PCA was performed combining MiP, MaP, BD and SRP data, and were named soil structure principal components (SS.PCs), resulting in a KMO score of 0.59 with a p-value of  $< 0.0001$  in Bartlett's sphericity test, with three principal components presenting eigenvalues higher than 1 (Figure 4abc). The second PCA represents the soil chemical attributes (SC.PCs), except P and K data, which had to be removed to achieve a  $KMO \geq 0.5$ . Two principal components were required to represent soil chemical data (Figure 4d), with a KMO value of 0.50 and a Bartlett's p-value  $< 0.0001$ . The third PCA was applied to yield components data (YC.PCs), with the RE variable removed to achieve a KMO of 0.63 and Bartlett's test p-value  $< 0.0001$ , and two principal components to represent the dataset (Figure 4e). A few other variables were not submitted to PCA, like soil texture and biomass attributes, either for their singular importance in explaining water dynamics or for not being composed of enough variables to be analyzed using PCA.

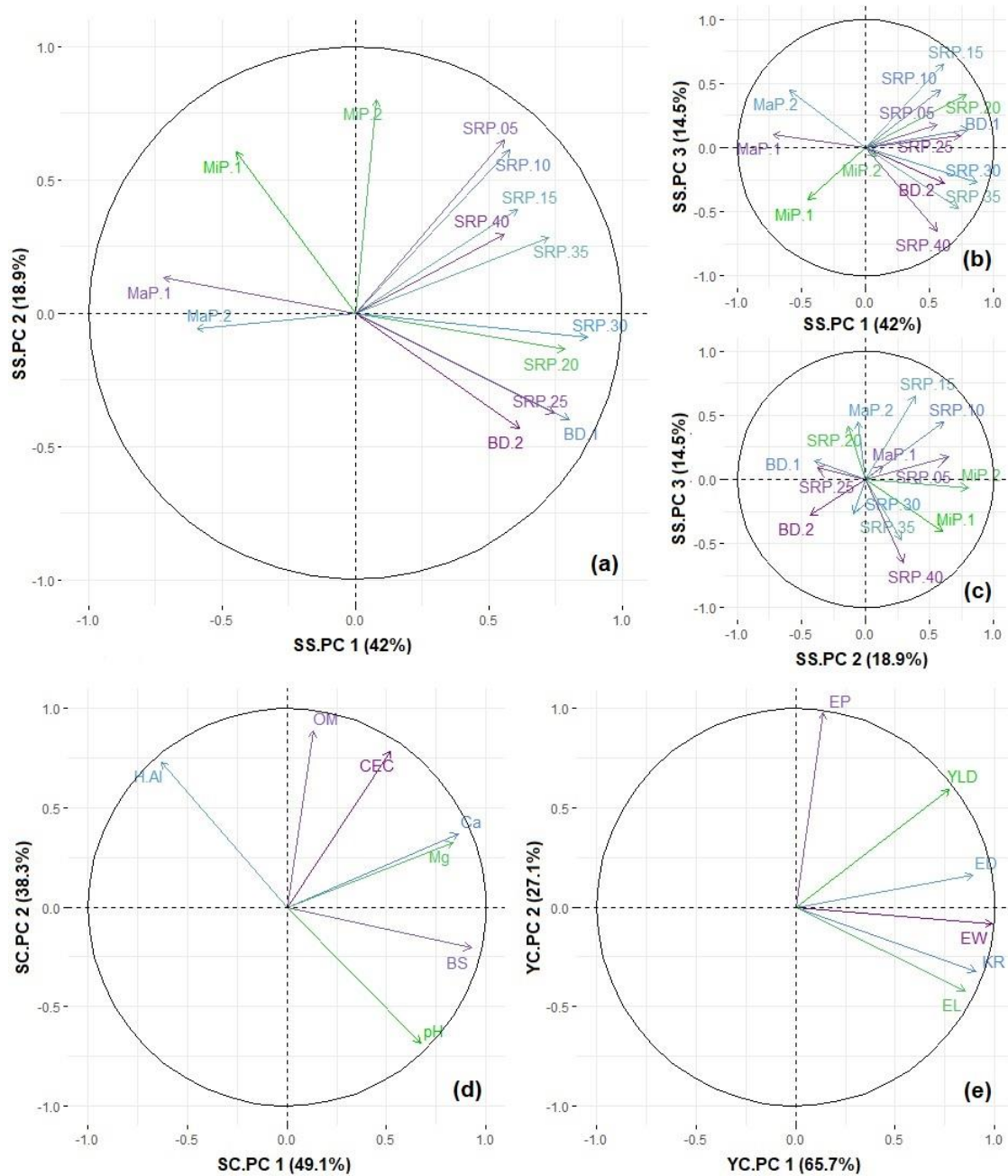


**Figure 4.** Biplots of the loadings from PCA performed with soil structure attributes, considering PC1 with PC2 (a), PC1 with PC3 (b) and PC2 with PC3. Biplots of loadings from the first two PCs of soil chemical attributes (d) and plant yield variables (e).

The correlations between the PCs obtained with the original variables are presented in Table 2. The soil structure attributes better explained by SS.PC1, which explains 41.97 % of the total variance, were the BD, SRP, and MaP, while the SS.PC2 was mainly influenced by MiP and shallow SRP readings. Among the soil chemical variables, the SC.PC1 explained 49.14 % of the total variance and was better represented by Ca, Mg and BS, whereas the SC.PC2 contains more information regarding OM and CEC. The yield components had their total variance more concentrated in YC.PC1, representing 65.75 %, and containing the majority of the input variables, except the EP, mainly represented by YC.PC2.

**Table 2.** Principal components analysis results from soil structure and chemical attributes, and from yield components attributes.

| Soil Structure Attributes      |               |               |               | Soil Chemical Attributes       |               |               | Yield Components Attributes    |               |               |
|--------------------------------|---------------|---------------|---------------|--------------------------------|---------------|---------------|--------------------------------|---------------|---------------|
|                                | <i>SS.PC1</i> | <i>SS.PC2</i> | <i>SS.PC3</i> |                                | <i>SC.PC1</i> | <i>SC.PC2</i> |                                | <i>YC.PC1</i> | <i>YC.PC2</i> |
| <b>Eigenvalues</b>             | 5.88          | 2.65          | 2.03          | <b>Eigenvalues</b>             | 3.44          | 2.68          | <b>Eigenvalues</b>             | 3.95          | 1.63          |
| <b>Cumulative variance (%)</b> | 41.97         | 60.89         | 75.39         | <b>Cumulative variance (%)</b> | 49.14         | 87.43         | <b>Cumulative variance (%)</b> | 65.75         | 92.87         |
| Variables                      | Correlation   |               |               | Variables                      | Correlation   |               | Variables                      | Correlation   |               |
| <b>MiP<sup>1</sup></b>         | -0.45         | 0.60          | -0.41         | <b>pH</b>                      | 0.67          | -0.68         | <b>YLD</b>                     | 0.77          | 0.59          |
| <b>MaP<sup>1</sup></b>         | -0.72         | 0.13          | 0.10          | <b>OM</b>                      | 0.13          | 0.89          | <b>EP</b>                      | 0.14          | 0.98          |
| <b>BD<sup>1</sup></b>          | 0.80          | -0.40         | 0.15          | <b>Ca</b>                      | 0.86          | 0.37          | <b>KR</b>                      | 0.91          | -0.33         |
| <b>MiP<sup>2</sup></b>         | 0.08          | 0.80          | -0.07         | <b>Mg</b>                      | 0.84          | 0.32          | <b>EL</b>                      | 0.85          | -0.42         |
| <b>MaP<sup>2</sup></b>         | -0.59         | -0.06         | 0.45          | <b>H+Al</b>                    | -0.63         | 0.73          | <b>ED</b>                      | 0.89          | 0.16          |
| <b>BD<sup>2</sup></b>          | 0.61          | -0.43         | -0.28         | <b>CEC</b>                     | 0.52          | 0.78          | <b>EW</b>                      | 0.99          | -0.09         |
| <b>SRP<sub>.05 m</sub></b>     | 0.56          | 0.65          | 0.18          | <b>BS</b>                      | 0.93          | -0.21         |                                |               |               |
| <b>SRP<sub>.10 m</sub></b>     | 0.58          | 0.61          | 0.45          |                                |               |               |                                |               |               |
| <b>SRP<sub>.15 m</sub></b>     | 0.61          | 0.39          | 0.65          |                                |               |               |                                |               |               |
| <b>SRP<sub>.20 m</sub></b>     | 0.79          | -0.14         | 0.41          |                                |               |               |                                |               |               |
| <b>SRP<sub>.25 m</sub></b>     | 0.74          | -0.38         | 0.09          |                                |               |               |                                |               |               |
| <b>SRP<sub>.30 m</sub></b>     | 0.87          | -0.09         | -0.27         |                                |               |               |                                |               |               |
| <b>SRP<sub>.35 m</sub></b>     | 0.72          | 0.28          | -0.47         |                                |               |               |                                |               |               |
| <b>SRP<sub>.40 m</sub></b>     | 0.56          | 0.30          | -0.65         |                                |               |               |                                |               |               |

<sup>1</sup>0.15 m soil depth; <sup>2</sup>0.35 m soil depth.

Pearson correlations among the final variables are illustrated in Figure 5. As expected, CT was negatively correlated with almost all variables, indicating that higher temperature readings can be linked to lower values on these observations. However, the correlation values were usually low, not exceeding 0.55. The correlation between soil and plant water content, expressed by SVWC and SWS versus BRWC and BWC, was positive, with values between 0.49 and 0.67, demonstrating that the amount of water in the soil and plants are somewhat related.

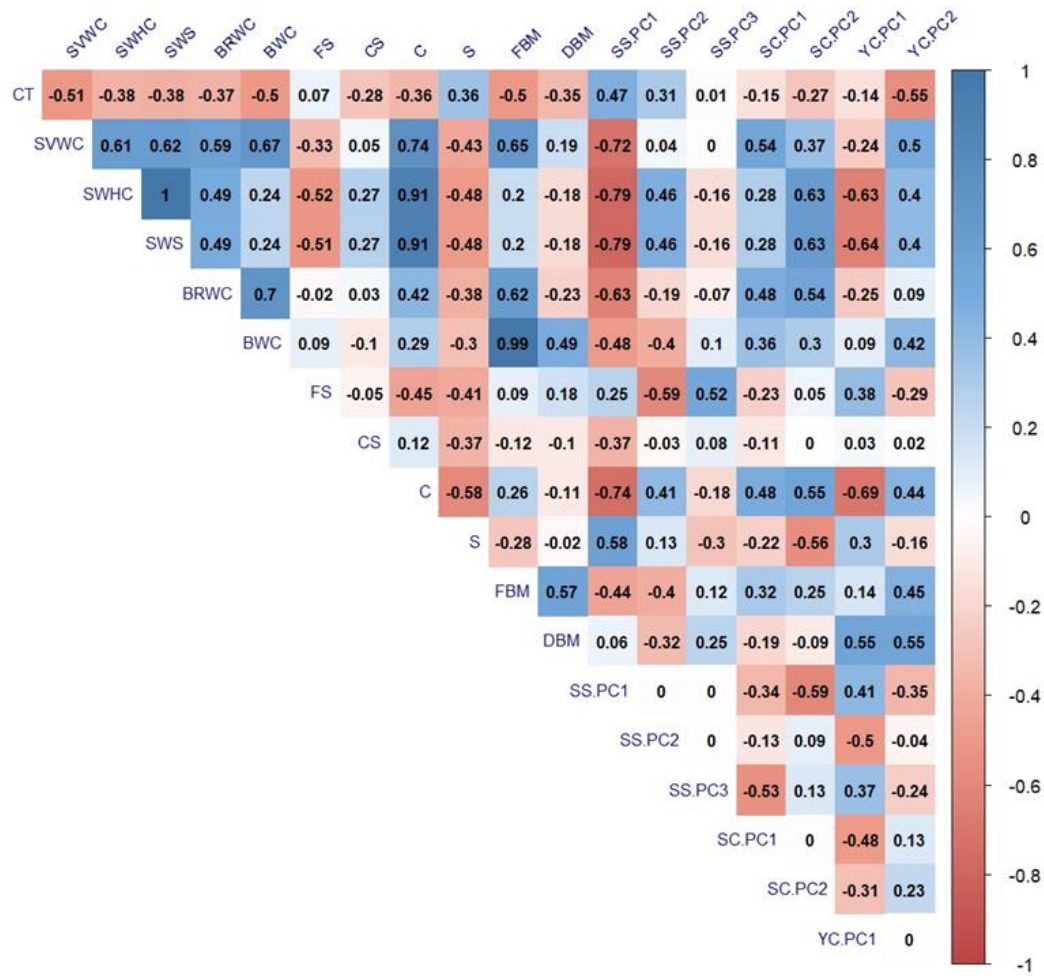


**Figure 5.** Pearson correlation matrix from attributes obtained at the sampling locations along with the principal components variables generated.

In order to test the feasibility of predicting the water content in soil and plants using CT information, we first implemented simple linear regressions with SVWC, SWS, BRWC and BWC as independent variables (Figure 6). The results showed that only the regressions models from SVWC and BWC were statistically significant, with p-values lower than 0.05 in the F-test, and coefficient of determination ( $R^2$ ) of 0.26 and 0.25, respectively.

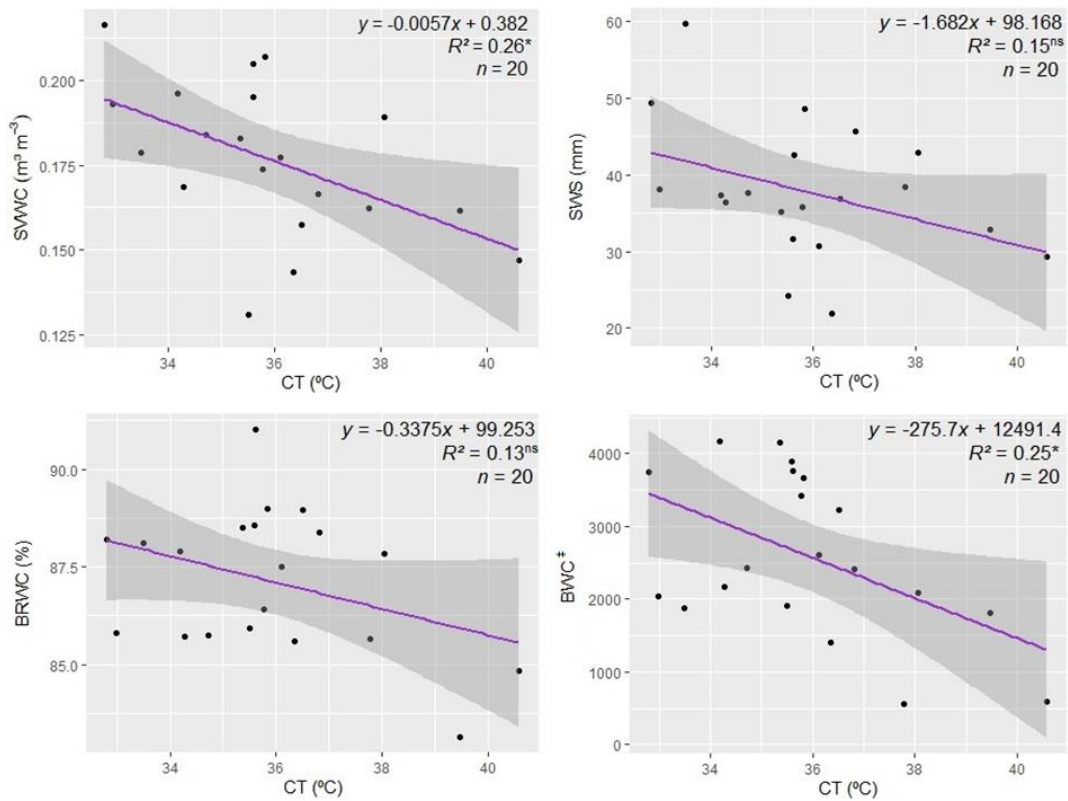


**Figure 6.** Simple linear regression models obtained between CT and dependent variables representing soil (SVWC and SWS) and plant (BRWC and BWC) water status. ‡ Box-Cox transformed ( $\lambda = 2.69$ ); \* p-value < 0.05 in the F-test; <sup>ns</sup> not significant in the F-test (p-value  $\geq 0.05$ ).

Moreover, the results from the stepwise multiple linear regression models obtained with the aforementioned independent variables associating CT with other attributes are listed in Table 3. To assess the soil water content, the independent variables included the PCs from soil structure and chemical attributes, along with soil texture variables and CT. When considering SVWC as the dependent variable, the model achieved an  $R^2$  of 0.83 without including CT, selecting the following variables as predictors (p-value  $\leq 0.1$ ): C, S, SS.PC2, SS.PC3 and SC.PC1. On the other hand, the model generated for SWS included CT as a predictor (p-value = 0.03) along with S, SS.PC1, SS.PC2, SS.PC3 and SC.PC2, yielding an  $R^2$  of 0.94. When CT was reversed as the independent variable, the  $R^2$  decreased to 0.38, with C and SS.PC3 being selected by the stepwise procedure.

The models used to assess the plant water status were tested with CT, DBM, YC.PC1 and YC.PC2 as independent variables. When testing BRWC as the dependent variable, the model was not statistically significant, with a p-value lower than 0.05 on the F-test. The BWC model, however, passed the F-test, resulting in an  $R^2$  of 0.25 with CT being selected as the only predictor variable. Finally, when CT was tested as the dependent variable, an  $R^2$  of 0.30 was obtained, with the YC.PC2 selected as the independent variable.

**Table 3.** Stepwise multiple linear regression results.

| Independent variables (x) | Dependent variable (y)    |                          |                           |                          |          |                        |
|---------------------------|---------------------------|--------------------------|---------------------------|--------------------------|----------|------------------------|
|                           | SVWC                      |                          | SWS                       |                          | CT       |                        |
|                           | Estimate                  | p-value                  | Estimate                  | p-value                  | Estimate | p-value                |
| CT                        |                           |                          | -0.889                    | 0.03 *                   |          |                        |
| FS                        |                           |                          |                           |                          |          |                        |
| CS                        |                           |                          |                           |                          |          |                        |
| C                         | 4.94·10 <sup>-4</sup>     | 7.0·10 <sup>-4</sup> *** |                           |                          | -0.023   | 0.01 *                 |
| S                         | 2.25·10 <sup>-4</sup>     | 0.02 *                   | -0.028                    | 0.09 .                   |          |                        |
| SS.PC1                    |                           |                          | -1.794                    | 2.1·10 <sup>-4</sup> *** |          |                        |
| SS.PC2                    | -5.85·10 <sup>-3</sup>    | 0.03 *                   | 2.854                     | 7.3·10 <sup>-6</sup> *** | 0.655    | 0.02 *                 |
| SS.PC3                    | 9.06·10 <sup>-3</sup>     | 2.2·10 <sup>-3</sup> **  | -1.450                    | 6.9·10 <sup>-3</sup> **  |          |                        |
| SC.PC1                    | 4.64·10 <sup>-3</sup>     | 0.06 .                   |                           |                          |          |                        |
| SC.PC2                    |                           |                          | 0.810                     | 0.09 .                   |          |                        |
| Intercept                 | -6.26·10 <sup>-4</sup>    | 0.99                     | 74.27                     | 9.63·10 <sup>-5</sup>    | 42.296   | 1.47·10 <sup>-12</sup> |
| R <sup>2</sup> multiple   | 0.83                      |                          | 0.94                      |                          | 0.38     |                        |
| R <sup>2</sup> Adjusted   | 0.77                      |                          | 0.91                      |                          | 0.31     |                        |
| F-test (p-value)          | 5.33·10 <sup>-5</sup> *** |                          | 4.17·10 <sup>-7</sup> *** |                          | 0.02 *   |                        |
| Shapiro-Wilk (p-value)    | 0.97                      |                          | 0.29                      |                          | 0.30     |                        |

| Independent variables (x) | Dependent variable (y) |         |          |                         |          |                         |
|---------------------------|------------------------|---------|----------|-------------------------|----------|-------------------------|
|                           | BRWC                   |         | BWC‡     |                         | CT       |                         |
|                           | Estimate               | p-value | Estimate | p-value                 | Estimate | p-value                 |
| CT                        |                        |         | -275.70  | 0.03 *                  |          |                         |
| DBM                       |                        |         |          |                         |          |                         |
| YC.PC1                    |                        |         |          |                         |          |                         |
| YC.PC2                    |                        |         |          |                         | -0.840   | 0.01 *                  |
| Intercept                 |                        |         | 12491.4  | 7.0·10 <sup>-3</sup> ** | 35.893   | 2·10 <sup>-16</sup> *** |
| R <sup>2</sup> multiple   | -                      |         | 0.25     |                         | 0.30     |                         |
| R <sup>2</sup> Adjusted   | -                      |         | 0.20     |                         | 0.26     |                         |
| F-test (p-value)          | ns                     |         | 0.03 *   |                         | 0.01 *   |                         |
| Shapiro-Wilk (p-value)    | -                      |         | 0.13     |                         | 0.63     |                         |

\*\*\* p-value <0.001; \*\* p-value <0.01; \* p-value <0.05; . p-value <0.1; ns not significant in the F-test (p-value ≥0.05); ‡ Box-Cox transformed ( $\lambda = 2.69$ ).

### 3.4. Discussion

Since the main goal of the study was to assess the suitability of remotely sensed CT on predicting maize water status, the data acquisition and image processing used focused on delivering precise and accurate temperature measurements. According to Mesas-Carrascosa et al. (2018), accuracies within 1 °C are ideal when analyzing crop water status with thermal cameras, which is similar to the reported values obtained with the same instrument and methodology employed in our study, where an accuracy of 1.32 °C (RMSE) and R<sup>2</sup> of 0.99 were observed under equivalent conditions (Acorsi; Gimenez; Martello, 2020).

Another important aspect regarding plant water status assessment using CT is the timing for data acquisition. In general, CT is a function of the evapotranspiration rate, which depends on the atmospheric evaporative demand and soil water storage (Khanal; Fulton; Shearer, 2017). Considering the VPD of 1.96 kPa measured during image acquisition, the meteorological condition was not restricting the evapotranspiration rate of the plants (O'Toole & Real, 1986; Gholinpoor et al., 2012; Yang et al., 2012) and therefore, CT would be mainly influenced by the soil water status. Results from the 10-day soil water balance calculated with SWHC adjusted for each sampling location revealed a water deficiency between 3.0 and 5.8 mm during this period, which was confirmed by the soil sampling carried out while aerial images were taken. The SVWC results varied from 0.13 to 0.22 m<sup>3</sup> m<sup>-3</sup> and compared well with SVWC values at the permanent wilting point (1,500 kPa), which according to the pedotransfer function employed to estimate SWHC, varies between 0.12 and 0.20 m<sup>3</sup> m<sup>-3</sup> among the sampling locations.

As a result, the soil water deficiency combined with thermal imagery carried out at midday, which is the time of the day that leaf water potential and stomatal conductance tend to be the lowest resulting in maximum expression of stress (Alchanatis, et al., 2010; Bellvert, et al., 2014), yielded temperature readings between 32.81 and 40.58 °C. Similar values were observed by DeJonge et al. (2015) when assessing maize water stress using CT in northern Colorado – USA, where the treatments with higher induced water stress presented average temperature of 31°C, ranging up to 39 °C during the vegetative stage. Moreover, Zhang et al. (2019) also obtained corresponding results while assessing different levels of irrigation in maize during late vegetative stage in China, with CT readings varying from 33.2 to 40.1 °C on treatments where irrigation restriction was applied.

Analyzing the Pearson correlation values between CT and attributes from soil that are linked to water retention, the highest value was obtained for SS.PC1 ( $r = 0.47$ ), which is primarily connected with SRP ( $r = 0.56 - 0.87$ ), BD ( $r = 0.61 - 0.80$ ) and MaP ( $r = -0.59 - -0.80$ ), followed by clay ( $r = -0.36$ ) and silt ( $r = 0.36$ ) content. These variables were well correlated with SVWC, presenting Pearson correlation values of -0.72, 0.74 and -0.43, respectively, and with SWS, where SS.PC1 yielded a correlation of -0.79, and clay and silt with 0.91 and -0.48, respectively. The results corroborate with the simple linear regression model obtained plotting CT against SVWC, where the linear relationship was statistically significant with an R<sup>2</sup> of 0.26, demonstrating that CT tends to increase when soil water content is reduced. The correlation was weaker in comparison to the values reported by Zhang et al. (2019), in which the linear regression models between SVWC at 0 – 0.2 m soil depth and CT yielded R<sup>2</sup> values between 0.40 and 0.53. The higher R<sup>2</sup> values can be explained by the treatments tested in the study, where five levels of irrigation were applied, from fully irrigated to severe deficit irrigation, resulting in a wider amplitude of soil water content during the assessment which contributed to obtaining regression models with well-distributed points favoring higher correlation values. Moreover, the second linear regression model obtained combining SWS and CT was not statistically significant (R<sup>2</sup> = 0.15), meaning that temperature increases do not always reflect lower SWS values. Although the result corresponds with the R<sup>2</sup> of 0.14 obtained by DeJonge et al. (2015) when plotting maize CT against SWS measurements throughout the growing season, it is worth highlighting that SWS was derived from a soil water balance model that is function of SWHC values estimated by a pedotransfer model and input meteorological variables predicted by NASA/POWER, which can introduce uncertainties to SWS measurements.

Despite the moderate to weak correlation values observed by Zhang et al. (2019) and DeJonge et al. (2015) when relating CT with soil water status variables, both studies reported higher correlation values when comparing CT with plant water stress indicators, such as stomatal conductance and leaf water potential, with R<sup>2</sup> values between 0.76 and 0.89. These results demonstrate that plant water stress can be more sensitive and responsive

than soil water status when using CT as a proxy. In our study, plant water status was assessed based on indirect indicators, which express the absolute (BWC) and relative (BRWC) amount of water present in the biomass. These variables showed variation on correlations with soil water indicators ( $r = 0.24 - 0.67$ ), but when plotted against CT in the linear regression analysis only BWC was statistically significant with an  $R^2$  of 0.25. This result can be explained by the stomatal regulation in response to the environment, which in this case is responsible to prevent water loss by reducing the stomatal conductance (Jones, 1992; Chaves et al., 2003). This way, an onset drought stress might not be able to change the biomass relative water content since plants can restrict water loss, and that can be clearly observed when analyzing the coefficient of variation of 2.11 % from BRWC data. Although BWC is also subject to this issue, it is not normalized by FBM, which corroborates to a wider range of values ( $CV = 18.8\%$ ). As a result, the absolute mass of water in biomass increases proportionally to FBM ( $r = 0.99$ ), while the biomass accumulation is a response to environment factors during plant growth, such as water availability. For this reason, we believe that sampling locations with higher BWC were less subject to water stress during crop development as a reflect of soil water status over time, and that can be verified by the Pearson correlation of 0.67 between BWC and SVWC. Therefore, BRWC and BWC are more suitable to assess long-term drought stress and might not match the onset plant water stress detectable through CT, which is usually verified based on leaf water potential and stomatal conductance (Baluja et al., 2012; Zarco-tejada et al., 2013; Turner et al., 2014).

When combined with other independent variables in multiple linear regression models predicting soil water content, CT was either not selected in the stepwise procedure or presented a lower significance in relation to other variables. Among these predictors, soil structure attributes (SS.PCs) and texture were the most significant ones, while CT was only selected in the SWS model with a significance of 0.03 (p-value) based on the T-test. Since the majority of variables directly involved in the soil water dynamic were included in these models, the contribution of CT was limited considering prediction models that were already performing well, with  $R^2$  values above 0.83.

Moreover, when CT was considered as the dependent variable, the stepwise procedure selected the clay content and SS.PC2 as the predictors of a regression model with an  $R^2$  of 0.38. Both variables are important to soil water retention, especially the clay content, which presented a Pearson correlation of 0.91 with SWHC, and SS.PC2 that mainly represents soil microporosity.

The results using plant water status variables presented virtually the same results observed in the simple linear regression, with a model not significant for BRWC and with CT selected as the only predictor for BWC. However, when CT was used as the independent variable YC.PC2 was selected as the single predictor ( $R^2 = 0.30$ ), which might reflect the long-term results of the drought stress detected by the thermal images, once YC.PC2 corresponds to the number of ears per plant and grain yield.

### 3.5. Conclusion

From UAV-based thermal imagery, we were able to generate a thermal orthomosaic representing the spatial variability of maize canopy temperature. Among the sampling locations, temperature readings varied from 32.81 to 40.58 °C, indicating different levels of plant drought stress across the field.

Exploring the hypothesis that canopy temperature is primarily a function of soil water storage, soil sampling was carried out to determine soil water content and other key variables directly related to soil water content. The results indicated that canopy temperature alone is not sufficient to predict soil water status accurately due to the low correlation values observed in our study ( $R^2 \leq 0.26$ ). Alternatively, the performance of soil water

status prediction was substantially increased when thermal data was associated with soil physical attributes ( $R^2 \leq 0.94$ ), demonstrating a combination that can be used as an in-season tool for onset drought stress assessments. Although canopy temperature was well correlated with a few plant variables, our conclusions are limited because these attributes reflect long-term drought stress, demanding more studies with intensive assessment throughout the growing season.

## References

- Acorsi MG, Gimenez LM, Martello M (2020) Assessing the performance of a low-cost thermal camera in proximal and aerial conditions. **Remote Sensing** 12:3591
- Alchanatis V, Cohen Y, Cohen S, Moller M, Sprinstin M, Meron M, Tsipris J, Saranga Y, Sela E (2010) Evaluation of different approaches for estimating and mapping crop water status in cotton with thermal imaging. **Precision Agriculture** 11:27-41
- Alvares CA, Stape JL, Sentelhas PC, Gonçalves JDM, Sparovek G (2013) Köppen's climate classification map for Brazil. **Meteorologische Zeitschrift** 22: 711-728
- Anderson DB (1936) Relative humidity or vapor pressure deficit. **Ecology** 17:277-282
- Aubrecht, DM, Helliker BR, Goulden ML, Roberts, DA, Still, CJ, Richardson, AD (2016) Continuous, long-term, high-frequency thermal imaging of vegetation: Uncertainties and recommended best practices. **Agricultural and Forest Meteorology** 228:315-326
- Baluja J, Diago MP, Balda P, Zorer R, Meggio F, Morales F, Tardaguila J (2012) Assessment of vineyard water status variability by thermal and multispectral imagery using an unmanned aerial vehicle (UAV). **Irrigation Science** 30:511-522
- Bellvert J, Zarco-Tejada PJ, Girona J, Fereres E (2014) Mapping crop water stress index in a "Pinot-noir" vineyard: Comparing ground measurements with thermal remote sensing imagery from an unmanned aerial vehicle. **Precision Agriculture** 15:361-376
- Berni JAJ, Zarco-Tejada PJ, Suarez L, Fereres E (2009) Thermal and narrowband multispectral remote sensing for vegetation monitoring from an unmanned aerial vehicle. **IEEE Transactions on Geoscience and Remote Sensing** 47:722-738
- Bian J, Zhang Z, Chen J, Chen H, Cui C, Li X, Chen S, Fu Q (2019) Simplified Evaluation of Cotton Water Stress Using High Resolution Unmanned Aerial Vehicle Thermal Imagery. **Remote Sensing** 11:267
- Chaves MM, Maroco JP, Pereira J (2003) Understanding plant responses to drought – from genes to the whole plant. **Functional Plant Biology** 30:239-264
- Crusiol LGT, Nanni MR, Furlanetto RH, Sibaldelli RNR, Cezar E, Mertz-Henning LM, Nepomuceno AL, Neumaier N, Farias JRB (2020) UAV-based thermal imaging in the assessment of water status of soybean plants. **International Journal of Remote Sensing** 41:3243-3265
- DeJonge KC, Taghvaeian S, Trout TJ, Comas LH (2015) Comparison of canopy temperature-based water stress indices for maize. **Agricultural Water Management** 156:51-62
- Elsayed S, Elhoweity M, Ibrahim HH, Dewir YH, Migdadi HM, Schmidhalter U (2017) Thermal imaging and passive reflectance sensing to estimate the water status and grain yield of wheat under different irrigation regimes. **Agricultural Water Management** 189:98-110
- Fedoroff NV, Battisti DS, Beachy RN, Cooper PJ, Fischhoff DA, Hodges CN, Zhu JK (2010) Radically rethinking agriculture for the 21st century. **Science** 327:833-834

- Fridgen JJ, Kitchen NR, Sudduth KA, Drummond ST, Wiebold WJ, Fraisse C (2004) Management Zone Analyst (MZA) Software for Subfield Management Zone Delineation. **Agronomy Journal** 96:100-108
- Fridgen JJ, Kitchen NR, Sudduth K.A (2000) Variability of soil and landscape attributes within sub-field management zones. **Proceedings of the 5th Conference on Precision Agriculture** 19:1-16
- Gago J, Douthe C, Coopman RE, Gallego PP, Ribas-Carbo M, Flexas J, Medrano H (2015) UAVs challenge to assess water stress for sustainable agriculture. **Agricultural water management** 153:9-19
- Gautan D, Pagay V (2020) A review of current and potential applications of remote sensing to study the water status of horticultural crops. **Agronomy** 10:140
- Gebbers R, Adamchuk VI (2010) Precision agriculture and food security. **Science** 327:828–831
- Gholipour M, Choudhary S, Sinclair TR, Messina CD, Cooper M (2013). Transpiration response of maize hybrids to atmospheric vapour pressure deficit. **Journal of Agronomy and Crop Science** 199:155-160
- Heiskanen J, Makitalo K (2002) Soil water-retention characteristics of Scots pine and Norway spruce forest sites in Finnish Lapland. **Forest Ecology and Management** 162:137-152
- Idso SB, Jackson RD, Pinter PJ, Reginato RJ, Hatfield JL (1981) Normalizing the stress-degree-day parameter for environmental variability. **Agricultural Meteorology** 24:45-55
- Iqbal J, Thomasson JA, Jenkins JN, Owens PR, Whisler FD (2005) Spatial Variability Analysis of Soil Physical Properties of Alluvial Soils. **Soil Science Society of American Journal** 69:1338-1350
- Jackson RD, Idso SB, Reginato RJ, Pinter PJ (1981) Canopy temperature as a crop water stress indicator. **Water Resources Research** 17:1133–1138
- Jones HG (1992) Plants and microclimate. **Cambridge University Press** pp.428
- Jones HG (2004) Irrigation scheduling: advantages and pitfalls of plant-based methods. **Journal of Experimental Botany** 55:2427-2436
- Kelly J, Kljun N, Olsson P-O, Mihai L, Liljeblad B, Weslien P, Klemedtsson L, Eklundh L (2019) Challenges and best practices for deriving temperature data from an uncalibrated UAV thermal infrared camera. **Remote Sensing** 11:567
- Khanal S, Fulton J, Shearer S (2017) An overview of current and potential applications of thermal remote sensing in precision agriculture. **Computers and Electronics in Agriculture** 139:22-32
- Klemas VV (2015) Coastal and environmental remote sensing from unmanned aerial vehicles: An overview. **Journal of Coastal Research** 31:1260-1267
- Lambers H, Chapin FS, Pons TL (2008) Growth and Allocation. In *Plant Physiological Ecology*. **Springer** pp.321-374.
- Lu Z, Percy RG, Qualset CO, Zeiger E (1998). Stomatal conductance predicts yields in irrigated Pima cotton and bread wheat grown at high temperatures. **Journal of Experimental Botany** 49:453-460
- Mulla DJ (2013) Twenty five years of remote sensing in precision agriculture: key advances and remaining knowledge gaps. **Biosystems Engineering** 114:358-371
- Maes WH, Steppe K (2019) Perspectives for remote sensing with unmanned aerial vehicles in precision agriculture. **Trends in Plant Science** 24:152-164
- Matese A, Baraldi R, Berton A, Cesaraccio C, Di Gennaro SF, Duce P, Facini O, Mameli MG, Piga A, Zaldei A (2018) Estimation of Water Stress in grapevines using proximal and remote sensing methods. **Remote Sensing** 10:1-16

- Mesas-Carrascosa FJ, Pérez-Porras F, de Larriva JEM, Frau CM, Agüera-Vega F, Carvajal-Ramírez F, Martínez-Carricondo P, García-Ferrer A (2018) Drift correction of lightweight microbolometer thermal sensors on-board unmanned aerial vehicles. **Remote Sensing** 10:615
- Minasny B, McBratney AB, Whelan BM (2006) Vesper version 1.6. **The University of Sydney**
- Mulla DJ, McBratney AB (2001) Soil spatial variability. In *Soil Physics Companion*. **CRC Press** pp.343-373
- Odeh IOA, McBratney AB, Chittleborough DJ (1992) Soil pattern recognition with fuzzy-c-means: application to classification and soil– landform interrelationships. **Soil Science Society of America Journal** 56:505-516
- O'Toole JC, Real JG (1986) Estimation of Aerodynamic and Crop Resistances from Canopy Temperature. **Agronomy journal** 78:305-310
- R Core Team (2020) R: A Language and Environment for Statistical Computing. Available online: [www.rproject.org](http://www.rproject.org) (accessed on 17 December 2020).
- Radoglou-Grammatikis P, Sarigiannidis P, Lagkas T, Moscholios I (2020) A compilation of UAV applications for precision agriculture. **Computer Networks** 172:107148.
- Rossi M (2017) Mapa pedológico do Estado de São Paulo: revisado e ampliado. **Instituto Florestal** pp.118
- Sobieraj JA, Elsenbeer H, Cameron G (2004) Scale dependency in spatial patterns of saturated hydraulic conductivity. **Catena** 55:49-77
- Teixeira PC, Donagemma GK, Fontana AI, Teixeira WG (2017) Manual de métodos de análise de solo. **Embrapa Solos Brasília** pp.573
- Thornthwaite CW, Mather JR (1955) The Water Balance. **Climatology** 4:1
- Tomasella J, Hodnett MG, Rossato L (2000) Pedotransfer functions for the estimation of soil water retention in Brazilian soils. **Soil Science Society of America Journal** 64:327-338
- Tremocoldi WA, Brunini O (2008) Caracterização agroclimática das unidades da Secretaria de Agricultura e Abastecimento do Estado de São Paulo: Capão Bonito e região. **Instituto Agrônomo de Campinas** pp.30
- Turner D, Lucieer A, Malenovsky Z, King DH, Robinson SA (2014) Spatial co-registration of ultra-high resolution visible, multispectral and thermal images acquired with a micro-UAV over Antarctic moss beds. **Remote Sensing** 6:4003-4024
- Yang Z, Sinclair TR, Zhu M, Messina CD, Cooper M, Hammer GL (2012) Temperature effect on transpiration response of maize plants to vapour pressure deficit. **Environmental and Experimental Botany** 78:157-162
- Zarco-Tejada PJ, González-Dugo V, Berni JAJ (2012) Fluorescence, temperature and narrow-band indices acquired from a UAV platform for water stress detection using a micro-hyperspectral imager and a thermal camera. **Remote Sensing of Environment** 117:322-337
- Zarco-Tejada PJ, González-Dugo V, Williams LE, Suárez L, Berni JÁ, Goldammer D, Fereres E (2013) A PRI-based water stress index combining structural and chlorophyll effects: Assessment using diurnal narrow-band airborne imagery and the CWSI thermal index. **Remote Sensing of Environment** 138:38-50
- Zhang L, Niu Y, Zhang H, Han W, Li G, Tang J, Peng X (2019) Maize canopy temperature extracted from UAV thermal and RGB imagery and its application in water stress monitoring. **Frontiers in Plant Sciences** 10:1-18
- Zhou J, Khot LR, Boydston RA, Miklas PN, Porter L (2018) Low altitude remote sensing technologies for crop stress monitoring: a case study on spatial and temporal monitoring of irrigated pinto bean. **Precision Agriculture** 19:1-15